

Pumped up Propulsion

Development of an electric rocket engine pump system for a rocket hopper

Leonie Büssenschütt

*Chair of Space Propulsion and Mobility
Technical University of Munich
Munich, Germany
leonie.buessenschuett@tum.de*

David Stadelbauer

*Chair of Space Propulsion and Mobility
Technical University of Munich
Munich, Germany
david.stadelbauer@tum.de*

Sven Julius Steinert

*Chair of Space Propulsion and Mobility
Technical University of Munich
Munich, Germany
0000-0003-4424-670X*

Thilo Witzel

*Chair of Space Propulsion and Mobility
Technical University of Munich
Munich, Germany
thilo.witzel@tum.de*

Abstract—This study presents the design of an electric pump power pack for the ASCENT Rocket Hopper main engine for cryogenic propellants (LOX, liquid propane). After introducing the relevant requirements and a subsequent trade space analysis, the detailed design of the oxidizer and fuel pumps is conducted. A custom electric motor with an integrated novel seal concept eliminating dynamic shaft seals is presented that has the potential to greatly reduce system complexity for small pumps. Numerical optimization schemes were used to find optimal designs of the hydraulic sections and the electric motor. The off-design characteristics of the system are explored as the engine will be capable of deep-throttling down to 30 % thrust.

Index Terms—rocket engine pump, cryogenics, electric motor, battery, deep-throttling

I. INTRODUCTION

The primary objective of this report is the presentation of the development of an electric turbopump (e-pump). The e-pump shall be integrated into a future rocket hopper developed by the Chair of Space Propulsion and Mobility of the Technical University of Munich. An e-pump is an essential part in a rocket engine since it plays a crucial role in supplying the necessary pressure for the combustion chamber. What distinguishes this development is the fact that the pump is electrically driven. In the past there have not been many electric e-pumps developed since they tend to have an unfavorable power to mass ratio mainly due to the heavy batteries required for the substantial energy. However, in recent years there have been some advancements, especially for smaller launchers [1], [2]. In this report many challenges like high rotational speeds, low weight, low mass flow, cryogenic compatibility, sealing methods and many more are discussed and a possible design solution is proposed.

II. DESIGN METHODOLOGY

A. Requirements

First of all, the requirements and boundary conditions shall be presented in order to provide a frame for the dimensioning.

TABLE I: E-pump Requirements

No.	Description
R01	The e-pump assembly should be of as few components as possible.
R02	The e-pump assembly should be easily manufacturable.
R03	The e-pump shall provide the required pressure for the required combustion chamber pressure.
R04	The e-pump assembly shall allow to throttle the engine.
R05	The hopper shall have an overall system margin of 20%.
R06	The rotational speed of the pump shall not exceed 45000 rpm.
R07	The eigenfrequencies of the pump shall not lie in the operational range of the pump.
R08	Standard components shall be used if possible.
R09	The e-pump shall be able to operate for 120s on full throttle.
R10	Provide a system voltage close to 48V for use of other teams.

Some of the requirements are provided by the Chair of Space Propulsion and Mobility. Additional boundary conditions were inflected upon the system by design limitations. In table I the requirements are listed.

The requirements on engine level were converted into numerical values for the required fluid input and output states (density, pressure, temperature) by the engine system group. The exact values are listed in table II as inputs for the pump design.

B. Trade Space Exploration

To start with the detailed calculations of the different subsystems an overall design architecture must be determined. A trade space analysis is conducted in which the most prominent design decisions are made. Five main parameters are chosen that have a large impact on the design.

The first design parameter is the **pump configuration**. Two options have been identified: either assembling both pumps on one shaft or creating two separate pumps. Advantages for the combined pump are the lighter and compacter construction. Additionally, motor, shaft, bearings, etc. are only needed once which may reduce the costs. On the other side, two separate

pumps lead to a better individual performance and easier development and enhancement possibilities. Another factor is the easier sealing concept. If both pumps are mounted on one single shaft there must be a very proficient sealing concept which keeps the LOX and propane from mixing in order to avoid ignition. In table XIII the advantages and disadvantages are summarized. Due to the numerous advantages of the two shaft configuration this configuration is selected for the e-pump.

The second parameter is the **motor**. A decision is made between buying an off the shelf motor or building one. Advantages for buying a motor off the shelf are the low costs, if a suitable motor is found as well as lower engineering effort, risks and lead times. Benefits for designing a motor is the high design flexibility as the performance can be optimized for the desired design points and the motor could be integrated into the pump system in a very efficient way. In addition, specific requirements such as cryogenic compatibility require nonstandard motor design, materials and manufacturing methods. In table XIV the advantages and additional disadvantages are summarized. The decision is made to design a custom motor due to the flexibility and the lack of a suitable motor on the market which could withstand the requirements listed in table I.

Another design decision is the **bearing concept** that shall be used in the e-pump. Three different options are explored: Ceramic bearings, hybrid bearings and superconducting magnetic bearings. The ceramic bearings have the most profound knowledge base, are well established (TRL9) and commercially available. Advantages of the hybrid bearings are the better reusability and the higher rotational speed limit. However, they are not flight proven and cannot be purchased easily. The last bearing type is the superconducting magnetic bearing. They are the most promising bearings in terms of losses and reusability, but require the highest development effort and cannot be purchased. In table XV the advantages and disadvantages are summarized. For the proposed e-pump design the ceramic bearings are chosen due to the fact that they can be bought and that they are the most common type of bearing in cryogenic pumps [3].

The next design decision is the **battery chemistry** which shall be used for the energy storage. Four different types are compared namely Lithium Iron Phosphate (LiFePO₄), Lithium-Titanium-Oxide (LTO), Lithium-Polymer (LiPo) and Li-Ion: INR (LiNiMnCoO₂). LiFePO₄ is the safest, cheap, has a high thermal stability and the longest cycle life, but its energy and power density are poor. LTO has the highest power density, the fastest charge rate and the lowest self-discharge rate, however is hardly accessible and has a high cost. LiPo batteries have a high power density and are the most flexible in shape and size, while having shorter life cycles. Li-Ion batteries offer the biggest product range with different power densities and are the widest adopted. In table XVI the arguments for and against each type are summarized. For the e-pump battery the Li-Ion: INR (LiNiMnCoO₂) was selected since it is the most modular and high power versions

which suit the requirements for the e-pump, which are more demanding on power rather than energy.

The last design decision is the **battery cooling concept**. Two concepts are compared: One with active battery cooling and one without it. An advantage of the active cooling concept is that higher currents can be drawn from the same cells which could reduce the numbers of cells needed for the same power. However, this adds complexity to the system and active regulation of the system is necessary, which is also adding mass. The concept of a battery without active cooling works by simply using more battery cells so that the heat generation is reduced by a reduced current draw. The passive cooled setup is very simple and reliable, while on the down side it has an increased mass by approximately 1/3. In table XVII the two versions of the cooling concept are shown graphically and the advantages and disadvantages are listed. For the e-pump the system without active cooling is chosen due to its simplicity. Summarized, one can find all the design decisions in the morphological box in table XII.

C. Workflow Diagram

The design of the e-pump is divided into four different work packages to enable a continuous and simultaneous work flow. The four work packages are: Electromotor, power supply, pump geometry and assembly. Different dependencies between the work packages and the other subsystems are identified to generate an overview of the whole project. The calculations for each work package are implemented with Python. In figure 1 the work flow is shown graphically in form of a flow chart.

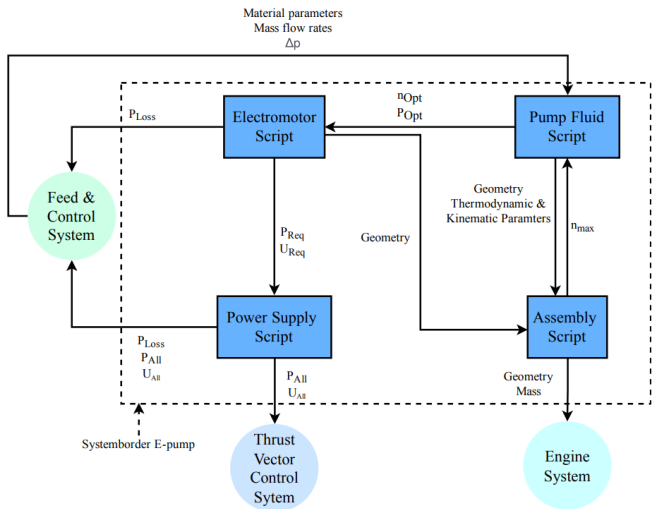


Fig. 1: Flow chart subsystem dependencies

The connection between each of the work packages are marked with the respective parameters that are transferred from one package to the other. The subsystems "Engine System", "Thrust Vector Control System" and "Feed & Control System" have been identified to be the relevant systems with which data must be interchanged. The design process is iterative which can be seen for example between the "Pump Fluid Script" the

"Electromotor Script" and the "Feed & Control System" since they form a closed loop.

D. Centrifugal Pump

In general, the design process of hydraulic components (turbomachinery) can be separated into the following steps:

- 1) Calculation of main dimensions including blade angles applying 1D-methods and empirical correlations derived from statistical data and based on experience
- 2) Shaping of hydraulic contours and generating an initial 2D-/3D-design
- 3) Verification and/or optimization using numerical flow simulations (CFD)
- 4) Testing for verification (or calibration of numerical model and further optimization

The combined design approach of the pump impeller, vaneless and vaned diffuser is based on the iterative process described by Gambini et al. [4] (figure 12) and employs additional statistical data from [5], [6] and [7], especially for off-design performance prediction.

$$\omega_s = \frac{2\pi \cdot n}{60} \cdot \frac{\sqrt{V}}{(g \cdot \Delta H_s)^{\frac{3}{4}}} \quad (1)$$

A radial configuration (centrifugal pump) was preselected according to the specific speed (Eq. 1) as volumetric flow rate and total pressure rise (pump head) are fixed boundary conditions (input parameters) and the (maximum) required rotational speed was, in combination with the number of stages and considering the maximum allowed value given by other components (e.g., bearings), estimated using a simplified approach described by Humble et al. [8]. Additionally, based on those preliminary calculations, a multistage configuration consisting of two geometrically equal stages for the propane pump and a single-stage design for the oxygen pump were initially chosen and verified with the subsequently applied, more detailed design method (figure 12).

The (fluidic) boundary conditions at the interfaces of the e-pump subsystem are specified downstream by the required thrust chamber total pressure and propellant mass flow (engine thrust) and losses across feed lines, valves and the injector head, and upstream by again (small) losses in feed lines and valves, but mainly the selected tank pressures.

Table II summarizes those input parameters, the independent design variables, resulting (dependent) geometric, kinematic and thermodynamic parameters, and (material) constants. In general, losses were assumed to decrease with the square of the rotational speed according to the scaling laws for the pump head [6]:

$$H_a = H_M \cdot \left(\frac{n_a}{n_M} \right)^2 \cdot \left(\frac{D_a}{D_M} \right)^2 \cdot \frac{z_{st,a}}{z_{st,M}} \cdot \frac{\eta_{h,a}}{\eta_{h,M}} \quad (2)$$

Further, the flow rate scales proportionally, the net positive suction head (NPSH) equivalent to the head quadratically and

the required pump power with the third power of the rotational speed.

The operational envelope of the pump is mainly limited by the hydrodynamic cavitation intensity exceeding the material-dependent cavitation resistance causing cavitation damage (or erosion) to high mass flows and by occurrence of rotating or axisymmetric stall (surge limit) to both high and low mass flows. The cavitation limit is determined according to the $NPSH_3$ -criterion which describes the point where the head of the suction impeller drops by 3%. An additional safety factor of 1.25 is applied and a minimum $\Delta NPSH_{min} = NPSH - NPSH_3 = 0.6 \text{ m}$ required following recommendations provided in [6].

Operational limitations due to stall are difficult to predict and various criteria such as the static pressure recovery coefficient in the vaneless diffuser ($c_{p,2-2S,crit} \gtrsim 0.7$) [7], the pressure recovery coefficient between impeller exit and diffuser throat ($c_{p,2-2S,q,crit} \gtrsim 0.4 - 0.45$) [9] or rough operational ranges depending on the flow parameter F (Eq. 3) with $1.2 - 1.1 \gtrsim F \gtrsim 0.6 - 0.4$ [6] have been proposed.

TABLE II: Pump boundary conditions, design variables, dependent parameters and constants

	Oxygen pump	Propane pump
Boundary conditions (input parameters)	$p_{t,in} = [3.2; 3.3] \text{ bar}$ $p_{t,out} = [12.3; 29.8] \text{ bar}$ $V = [0.16; 0.56] \text{ dm}^3/\text{s}$	$p_{t,in} = [3.4; 3.5] \text{ bar}$ $p_{t,out} = [12.5; 31.5] \text{ bar}$ $V = [0.12; 0.36] \text{ dm}^3/\text{s}$
Constants	$\rho_{Ox} = 1142 \frac{\text{kg}}{\text{m}^3}$ $k_s = 10 \mu\text{m}$ $T_{in} = 90 \text{ K}$	$\rho_{Prop} = 728.53 \frac{\text{kg}}{\text{m}^3}$
Design variables	$z, n, \phi, \psi, R \text{ (or } \xi\text{)}, \delta_t, \delta_h, \alpha_1, N_{b,R}, N_{b,S}, c_p$	
Dependent parameters (output parameters)	Geometric: $D_{1t}, D_{1h}, D_2, D_{2S}, D_3, D_{hyd,R}, D_{hyd,vaned}, b_1, b_2, b_{2S}, b_3, O_2, O_{2S}, L_{hyd,R}, L_{hyd,vaneless}, L_{hyd,vaned}, \beta_{2B}, r_{eq}, A_R, A_{R,opt}$ Kinematic: $\alpha_2, \beta_1, \beta_2, c_1, c_{1m}, c_{1u}, u_1, w_1, w_{1u}, w_{1q}, w_{1M}, \bar{w}_R, c_2, c_{2m}, c_{2u}, u_2, w_2, w_{2u}, \bar{w}_{vaneless}, c_{2S}, c_{2Su}, c_{2Sm}, c_{2Sq}, c_3, \mu_1, \mu_{2S}$ Thermodynamic: $p_1, p_2, p_{2S}, p_3, Z_{H,vaneless}, Z_{H,vaned}, Z_{H,S}, Z_{H,sf}, Z_{H,shock}, Z_{H,R}, Z_H, W, P, \eta_{hyd}, \eta_{hyd,R}$	

$$F = \frac{V/n}{(V/n)_{des}} \quad (3)$$

Due to those large uncertainties and the high dependency on the specific pump design, safe operation is assumed to still be possible for $F \gtrsim 0.5$ as the pump will not be operated at overload. This will have to be verified by numerical simulation and testing. Predicting off-design performance is mostly based on statistical data and experience due to the complexity of the relevant (3D) flow phenomena at such as recirculation (only at partload), flow separation and local stall [6]. The losses in the vaneless and vaned diffuser are estimated according to a polynomial of third order derived from empirical data for

multiple diffuser and volute pumps provided in [6], the slip factor scales with the third order polynomial given in [7] and the pressure recovery coefficient follows data measured on an impeller with $n_q = 33$ [6] which is about twice as high as for the designed oxygen pump at the best efficiency point (BEP) $n_{q,BEP} = 15.3$.

Finally, hyperparameter optimization capabilities within Optuna were employed to ensure that the resulting pump geometries fulfill various feasibility criteria (Sec. IX), their pressure recovery coefficient for the vaneless diffuser matches the corresponding optimal value calculated according to Eq. 23, and overall hydraulic efficiency is maximized. More information about the formulation of the optimization problem statement including design variables, constraints and objective function can be found in section X. For further details on the pump design process and the sizing of different components refer to chapter III-A.

E. Electric Motor

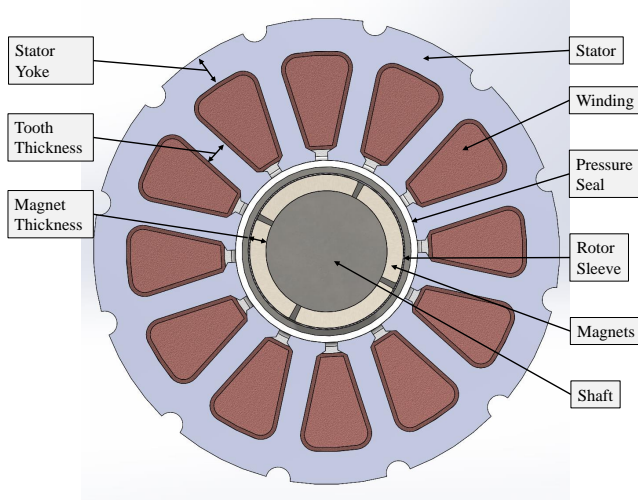


Fig. 2: Cut view of the proposed motor geometry

Because of the reasons named in chapter II-B, a custom electric motor is developed for both pumps. To increase commonality, reduce development effort and because the required maximum load (power, speed) is similar, one motor will be designed for both pumps. Because of its high gravimetric power density, high efficiency and readily available commercial control electronics, a brushless DC (BLDC) motor type is chosen [10]. This synchronous machine consists of a stator with a 3-phase AC winding creating a rotating magnetic field and a rotor consisting of permanent magnets.

In general, the process of designing an electrical machine is a complex task that includes considerations of three main disciplines: electromagnetic, thermal and mechanical. The main focus of this section is the electromagnetic design of the motor with regards to the power and speed demands to show feasibility of this pump concept. The thermal and mechanical framework is set by using experience and literature values, as is common in an early stage of development of an

electric machine. Because of the centrifugal load due to the high rotational speeds and the difficulty to glue in cryogenic environments, the magnets will be fixed with a carbon fibre (CFRP) sleeve.

The following section will give a brief overview (see figure 3) of the motor design process with more details in chapter XI.

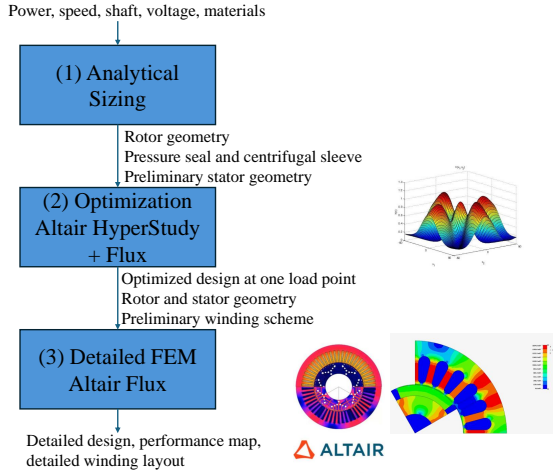


Fig. 3: Flowchart of the motor design process

1) Inputs: The main inputs for the motor design are the load point (speed, power) originating from the hydraulic design and the maximum phase voltage given by the inverter and the battery (values in table III). Since the motor will be used for both pumps, the load point is chosen with the maximum power and speed requirements of both pumps with a power reserve of 35 % to account for additional losses, that are neglected in this study (mechanical, gap flows, etc.):

$$P_{req} = \max(P_i) = 1760 \text{ W} \xrightarrow{+35\%} \approx 2400 \text{ W} \quad (4)$$

Furthermore, the minimal diameter of the shaft is given as a geometric boundary condition (BC). The phase voltage in RMS is limited by the DC voltage of the battery provided to the 3-phase inverter at the end of the flight:

$$U_{ph,rms} = \frac{U_{DC}}{\sqrt{2} \cdot \sqrt{3}} \quad (5)$$

The torque of the motor is a result of the required power and speed at the load point and is produced by the phase current through the winding turns roughly independent of the rotational speed. The rotating magnets induce a voltage (back-electromotive force, back-EMF) into the winding (Lenz rule) that opposes the current flow and increases with the speed and winding turn number. Thus, the speed of a machine is limited by the maximum available phase voltage. Since the winding losses (heat generation) scale quadratic with the phase current ($P = I^2 \cdot R$), it limits the thermal performance of the machine. In general, electrical machine design is linking thermal and electromagnetic design to find an optimum design that does not overheat at the specified load point. For simplification, a current density at the higher end of air-cooled machines

(acc. to [11]) is used to introduce thermal limitation into the design. This simplification is a standard used in electric motor pre-design and is also used in other studies (for example [11]).

TABLE III: Motor input parameters

Variable	Value	Unit
Power	2400	W
Speed	38000	rpm
Phase Voltage	20	Vrms
Shaft diameter	10	mm
Max current density	10	A/mm ²

2) *Analytical sizing:* This step approximates the dimensions and mass of the machine by utilizing analytical relations. The general design approach presented in [12] in combination with design rules in standard literature ([13] [14]) is followed in the Python script `main.py` in the electric motor section of the digital appendix. The dimension of the magnet retaining sleeve is calculated according to the design approach and material properties of CFRP in [15]. The seal between the rotor and stator has to withstand internal pressure generated by the pump. To reduce eddy current losses, it has to be non-conductive. PEEK is chosen as the material and the thickness of the cylindrical section is calculate with Barlow's formula [16]:

$$s = \frac{p \cdot d_m}{2 \cdot \sigma_{\text{allowed}}} \quad (6)$$

The output of this step is a preliminary geometry for the rotor and stator that serves as the initial configuration for the optimizer.

3) *Numerical simulations:* The detailed design of the stator and winding has to be carried out with finite element (FEM) software to achieve sufficient accuracy. The software FluxMotor by Altair is used to numerically solve for the magnetic field inside the motor. Furthermore, the losses inside the machine and thus the efficiency can only be accurately calculated with a detailed magnetic field distribution inside the motor. FluxMotor can also be connected to Altair's optimization tool HyperStudy to automatically explore the design space. Similar to the method proposed in [11], the following design targets for the optimization are to minimize mass and maximize efficiency:

$$f_{\text{obj}}(x) = \min(m, P_{\text{loss}}) \quad (7)$$

The boundaries regarding the operation in table III are enforced in the optimization. The optimizer can change the following variables (consult figure 2 for variable explanation):

- Rotor magnet thickness
- Stator iron geometry (tooth thickness, back-iron yoke thickness, length, outer diameter)
- Winding parameters

After the optimization has given an optimal design for one load point, a detailed FEM is set up to calculate the electromagnetic performance of the motor over its entire operational range. The outputs of this step are:

- Validation of optimized geometry performance
- Calculation of motor performance at off-design points
- Final motor design

F. Battery Pack

The design workflow of the battery pack and its electronics:

- Select specific battery cell type to match energy- to power-ratio
- Select BLDC driver by voltage and power capabilities to match motor requirements
- Determine battery voltage by system voltage and BLDC driver voltage
- Determine battery cell layout by variable voltage and power requirements
- Select a battery management system (BMS) based on battery requirements to complete the battery pack
- Determine battery pack specifications

The Battery is chosen to be custom configured by cells. This way the battery voltage and maximum discharge current are design parameters which can be set by other systems and the battery is configured accordingly. The design parameters for the battery pack are driven by the motor requirements on power and voltage and are cascaded back from the motor over the motor driver to the battery and then to its BMS. After the battery chemistry, the first design choice is the battery cell model, where its requirements can be fully determined by the mission profile and power demand alone. Essentially, different cells differ in energy- and power-density and the cell model is chosen which matches the energy to power ratio of the mission the closest. The BLDC driver is picked first to determine the upper limit on the systems voltage support. A further requirement on the design voltage is a system voltage close to 48V, from R10. The decision on the design voltage was then a compromise between these two values. Entering the design of the battery, the voltage and current capabilities are determined by the layout of cells connected in series or parallel. Due to the cell characteristics to feature a variable voltage depending on its state of charge, the battery voltage will vary over the time of flight. As the expected load is a constant power over the flight time, the combination of voltage and current drawn from the battery pack is time dependent. Due to a battery cell is being thermally limited by the discharge current, its maximum power has a constant current, but a variable voltage, resulting in the battery having also a variable power capability over the flight time. Either the lowest expected voltage can be determined by the used energy over the flight time or the battery's worst state. The fully depleted voltage, was taken as design constrain, as it provides additional margin against battery degradation during re-usability and robustness during non-nominal flights. The BMS protects the battery from over-current, under-voltage and also handles the charging process. The BMS itself must support the requirements on voltage and current. A suitable BMS is picked for the selected series layout and multiple BMS are combined to deliver the required current.

When all the components are selected, the battery pack characteristics over flight can be estimated and given as specification.

III. PROPULSION (SUB-)SYSTEM DESIGN

A. Centrifugal Pump

This section presents the optimized pump geometries for liquid oxygen (drawing F ("LOX Impeller + Diffuser") and figure 11) and propane, the corresponding geometric, kinematic and thermodynamic parameter values (table XVIII), and their respective performance characteristics (figure 4 and figure 14).

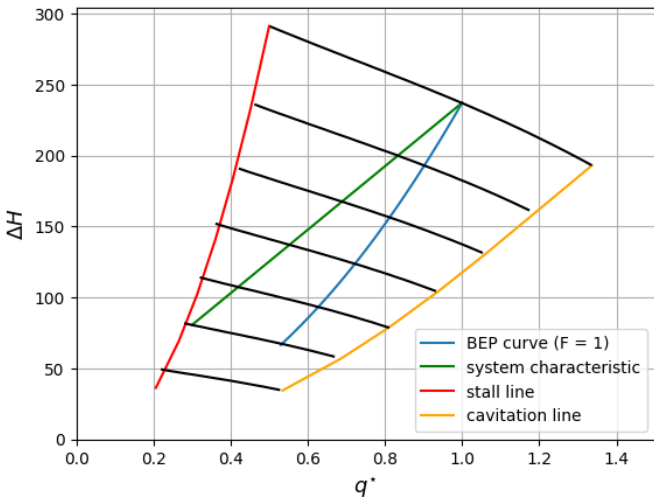


Fig. 4: Oxygen pump performance map

Operation is limited by the stall line (red) to small mass flows ($F < 1$) and the cavitation line (orange) towards high mass flows ($F > 1$), although critical flow separation and local stall may appear at overload even before the latter is reached. Due to the low vapor pressure of propane $p_{v,P} \approx 9.7 \cdot 10^{-9}$ bar ($p_{v,Ox} \approx 0.98$ bar) $NPSH > NPSH_3$ is fulfilled for every theoretically achievable flow parameter, therefore, operation of the propane pump at overload is limited solely by these unsteady flow phenomena. However, design for maximum efficiency at $q^* = 1$ ($F_N = 2400$ N) ensures operation strictly at $F \leq 1$ indicated by the system characteristic (green) "lying" to the left of the BEP curve (blue). The two operating points ($q^* = 0.3$ and $q^* = 1$) for each pump and the corresponding rotational speeds, flow parameters and power requirements (without mechanical losses and motor efficiency) are summarized in table IV.

Neglecting volumetric losses an overall hydraulic efficiency of 85.3% (LOX) and 74.1% (propane) for operation at the design point ($q^* = 1$) and 76.6% (70.9%) for throttled operation ($q^* = 0.3$) is achieved. figure 16 (LOX) and figure 15 (Propane) show the efficiency for different rotational speeds with their respective maxima at BEP ($F = 1$) as rotor losses were assumed to be constant and diffuser losses scaled with

the flow parameter.

Monotonically strictly decreasing pump characteristics (black) with $\partial H / \partial V < 0$ guarantee stable operation for constant rotational speeds.

TABLE IV: Rotational speed, hydraulic efficiency, flow parameter and power for oxygen and propane pump for design point and throttled operation

	$q^* [-]$	$n [rpm]$	$\eta_{hyd} [\%]$	$F [-]$	$P [W]$
Oxygen pump	0.3	20620	76.6	0.542	143
	1	38800	85.3	1	1760
Propane pump	0.3	18930	70.9	0.688	133
	1	36137	74.1	1	1403

B. Electric motor

The following section summarizes the results of the electric motor design. Overall, more than 250 configuration were calculated during the optimization procedure. The individual points are plotted in figure 5. The motor mass is plotted over the power with the color map representing the machine efficiency. The finalized design (referenced in table XIX in the appendix) is a compromise of mass and efficiency. It is an important parameter because it influences the motor heat generation and battery mass. A less efficient motor would thus result in a higher battery mass and may lead to overheating. Apart from the motor performance in the dedicated load point, the torque and power of the motor can be calculate over the entire speed range. The results are plotted in figures 6 and 19. The torque and power curves in figure 19 are given for the maximum phase current. Beyond 40000 rpm, the back-EMF generated by the magnets exceeds the voltage of the power supply. With an advanced control technique called field-weakening control, the permanent magnet flux can be reduced by controlling the stator current in a certain way [13, p. 465 f.]. This allows for operation beyond 40000 rpm while reducing the output torque thus resulting in an almost constant output power.

figure 6 plots the motor efficiency up to the maximum phase current and 75000 rpm and contains figure 19 as well as all possible operation points besides the design point. Efficiencies below 60 % are not plotted. This does not mean that the motor would not work at very low torque or speed. However, the motor should not be operated in this region for a prolonged time due to its inefficiency. Furthermore, the two operation points for the pumps (100 % and 30 % thrust case) are given in the plot for both propellants. The power/speed characteristic between the two load points is assumed linear for simplicity. It is apparent, that the operational regime of both pumps is well within the maximum efficiency region and the motor is not projected to be less efficient than 80 % during steady-state pump operation. Furthermore, the motor has a power excess to compensate for the losses currently not considered in the hydraulic design and ensures good pump operation, should the hydraulic section under perform on the test stand.

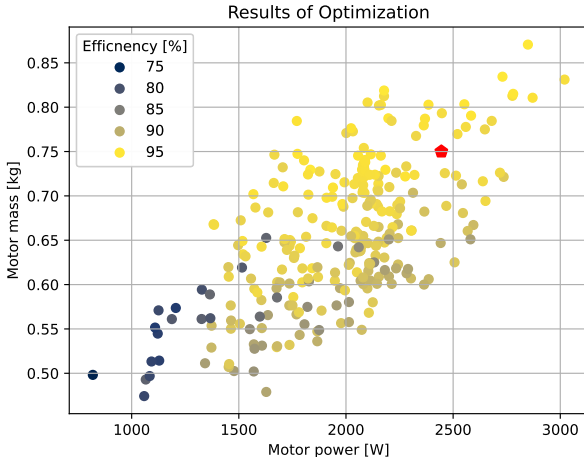


Fig. 5: Calculated configurations during optimization. The final motor is marked with the red pentagon.

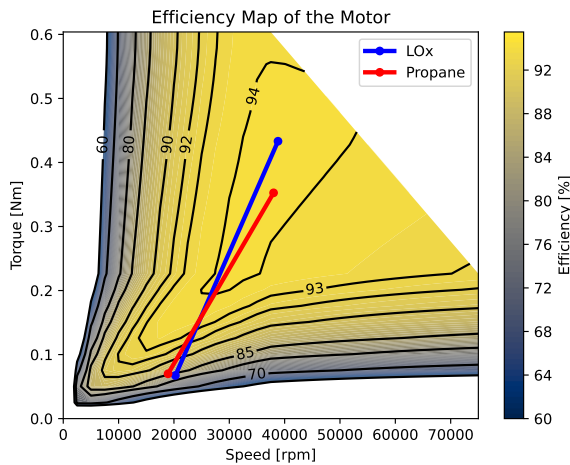


Fig. 6: Efficiency map of the final motor configuration.

C. Battery Pack

To select a suitable cell, first the cell size is picked to be 18650 cells, which are the most commonly used format with a great range of products. In table V is listed a comparison of 18650 cell models for high power applications from Samsung SDI, a well established manufacturer.

TABLE V: Battery cell model overview from Samsung INR

model nr.	U_n [V]	I_d [A]	$I_{d,p}$ [A]	C [mAh]	m [g]	$r_{E/P}$ [J/W]
INR18650-35E	3.6	8	13	3250	50	2105.0
INR18650-30Q	3.6	15		2900	48	501.3
INR18650-25S	3.6	25	100	2400	47	355.4

Reconsidering the requirement R09 from table I of the flight time $t_h = 120s$ into Equation 8, the cell model with the closest energy to power ratio $r_{E/P}$ is picked. Notably all of the available models are having a ratio higher than required,

which results in the battery to be bottle necked by its power capability while carrying excess energy. The closest ratio to the mission is offered by the INR18650-25S which is the selected cell model.

$$r_{E/P,req} = \frac{E_{req}}{P_{req}} = \frac{P_{req} \cdot t_h}{P_{req}} = t_h = 120 \frac{J}{W} \quad (8)$$

To configure a suitable layout of parallel and series connections, the target voltage is determined first. As the desired motor voltage is to be set as high as possible, the upper limit for the voltage was determined by the limits of the control signal conditioning BLDC-driver which is picked next. This driver is selected to be a commercial off the shelf BLDC driver, the MGM COMPRO HBC Motor Controller (HBCi10063)[17], which supplies up to 6 kW at maximum 63 V while featuring a very low mass of only 63 g.

To compromise this voltage with a system voltage close to 48V, the amount of cells connected in series S is selected. Due to this number being an integer, the battery cell voltage (min 2.8 V, max 4.2 V, nominal 3.6 V) can only be incremented in steps. Under nominal voltage in equation 9, the number of cells in series is $S = 14$ and the resulting voltages are min. 39.2 V, max. 58.8 V, nominal 50.4 V, which fits both under 63V for the maximum case, as well as close to 48V at the nominal point.

$$S = \lceil \frac{U_{target}}{U_{cell}} \rceil = \lceil \frac{48 V}{3.6 V} \rceil = 14 \quad (9)$$

To determine the number of strings put in parallel P_a , the power demand is taken as design input. All n power consuming units are the turbo-pumps with $P_1 = 1900 W$ for Oxygen and $P_2 = 1500 W$ for Propane, the thrust vector control with $P_3 = 345 W$, the pintle throttling with $P_4 = 28 W$, the valves with $P_5 = 10 W$ and the ignition system with $P_6 = 2 W$. The total sum from Equation 10 was rounded up with a high margin due to uncertainties about the real efficiencies of the turbo-pumps and its volumetric losses. This uncertainty amplifies through the motor as a shifted operating point would also reduce the efficiency of the motor and increase the power demand further, which is why a margin of 30% was applied.

$$P_{req} = \sum_{i=1}^n P_i = 3785 W \xrightarrow{+30\%} \approx 5000 W \quad (10)$$

As one cell can only be operated at maximum current of $I_d = 25A$ without cooling, the maximum power for one string at the lowest voltage of 39.2 V is 980 W which determines by equation 11 the number of strings to be put in parallel to be $P_a = 6$. It would be possible to design the battery more on edge with $P_a = 5$ or even $P_a = 4$, however this requires a well known power demand and pushes the batteries to their thermal limits.

$$P_a = \lceil \frac{P_{req}}{P_{string,max}} \rceil = \lceil \frac{5000 W}{I_d \cdot U_{min} \cdot S} \rceil = 6 \quad (11)$$

As the final missing part, a Battery Management System (BMS) is required to support the 14S configuration but also deliver the desired current. To feature a more modular design, multiple BMS are used, so that one unit of 14S and 2Pa is controlled by one BMS, resulting in 3 units with 3 BMS. The selected BMS is the JIABAIDA 10S-17S 80A model [18], which supports up to 80A each and also serves as charge controller to reuse the battery. If nothing modular or redundant is required and simplicity and mass savings are preferred, the BMS could also be simplified into one board. This concludes the selection of parts for the electric assembly and the complete battery pack can be specified by its discharge curve for the expected load case, which can be seen in figure 7. Under nominal flight with its required energy E_{req} , the battery pack is not nearly depleted and still features a rather high voltage, which is very favourable for the motors efficiency.

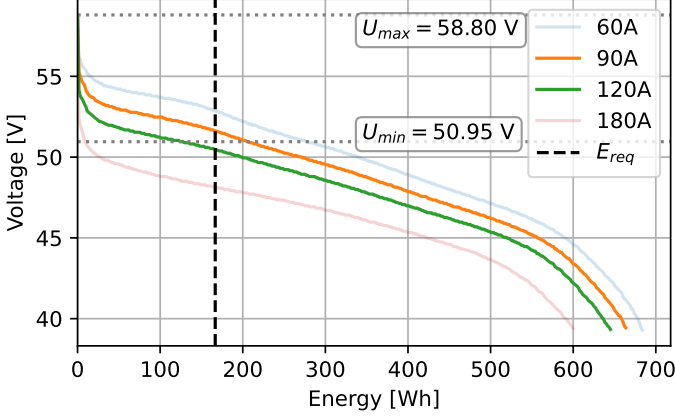


Fig. 7: Discharge curve of the battery pack

This discharge behaviour results in a variable voltage and current combination over the time of flight, which is illustrated in figure 22. The resulting battery pack specification of power, voltages, currents and energies is summarized in table VI.

TABLE VI: Battery pack specification

description	sign	value	unit
discharge voltage at 5kW	U_d, nom	58.80 .. 50.95	V
discharge current at 5kW	I_d, nom	85.0 .. 98.1	A
fully depleted voltage	U_{empty}	37.8	V
max continuous discharge current	$I_{d,max}$	150.0	A
max pulse discharge current	$I_{d,p}$	600.0	A
minimum power at $I_{d,max}$	P_{min}	5670	W
maximum power at $I_{d,max}$	P_{max}	8820	W
max pulse power at U_{min}	$P_{p,max}$	22.68	kW
ideally stored energy	E_{stored}	756.0	Wh
used energy during flight	E_{used}	166.7	Wh
loss energy at nominal discharge	E_{loss}	98.6	Wh
energy left after flight	E_{left}	490.8	Wh

The battery cells are mounted with plastic spacers and spot welded with Nickel strips, resulting in the 3D assembly in fig-

ure 23. The parts list is specified in table XX and the geometric containment is outlined by $300mm \times 150mm \times 100mm$.

D. Assembly

In order to assemble the e-pump some parts still need to be chosen and calculated. In the following, essential parts and concepts of the pump that have not been discussed yet are displayed.

Bearings The bearings are the main limitation for the rotational speed of the pump. Especially since the ceramic bearing type (which is sometimes also referred to as hybrid bearing) was chosen. It is essential to calculate the most important parameters for the bearings and cross check whether they fit with the parameters of the fluid components. The detailed calculations for the bearing design can be found in section VIII. The result of the bearing calculation is the determination of the bearing dynamic capacity C_{req} which was calculated to be 1.36kN for the LOX pump and 1.29 for the propane pump. With the help of these values the hybrid angular contact bearings and hybrid ball bearings from the company Gehrig® are selected. For the non-locating bearings two bearings are used of the type 696 are chosen [19]. Combined they have a bearing dynamic capacity of 1.86kN which is above the required value. These bearings can only take in the radial forces and thus for the locating angular bearing an back to back arrangement is chosen. This has the advantage that it creates a larger supporting basis and make the enables less tilting [20]. For the hybrid angular contact bearings the type 7000 is chosen which have bearing dynamic capacity of 3.02kN each [21]. The data sheets for each bearing can be found in the digital appendix.

Manufacturing methods Different manufacturing methods shall be used for the production of the parts.

- **3D Printing:** Volute, housing
- **CNC milling:** Impeller, diffuser
- **Welding:** Impeller, diffuser
- **Turning:** Shaft, housing, housing lid, impeller nut, pressure sleeve
- **Laser cutting:** Electric motor stator sheets

Assembly description A overall pump drawing can be found in F. A CAD rendering of the LOX pump is depicted in 11. In order to assemble the pump one must start at the motor. The permanent magnets must be glued on the shaft and the CFRP rotor sleeve must be place on top of it as an additional safety. After that the pressure ring shall be glided above the shaft followed by the coils and the stator geometry. Form both side the metall C-ring are inserted into the pressure ring to seal of the stator and the coils from the fluid. After that the hybrid ball bearings can be placed one after the other onto the shaft from the right side. In between the bearings the bearing ring must be placed. The bearings are secured with a locking ring. From the left side the first angular ball bearing can be placed onto the shaft. After that the housing lid can be put onto the shaft from the right side and the main housing is placed onto the shaft from the left. Both are connected via ten M4 bolts. The second angular ball bearing is placed on the

shaft followed by the grooved nut and the lock washer which fasten the bearings axially. Now the diffuser can be slid onto the shaft and the impeller can be placed behind it as well. The impeller is fixed via a custom made impeller nut. The diffuser can be fastened in the axial direction by placing the volute onto the shaft and combining the main housing with the volute on the flange via ten M3 bolts. Lastly, the four adapters from the Swagelok company are connected to the inlet, the end of the volute and the two ends of the cooling channels of the main housing. The overall mass of the LOX pump is **1.63 kg**.

E. Eigenfrequency Analysis

To evaluate the dynamic behaviour of the pump a eigenfrequency analysis of the LOX pump is conducted. Included in the analysis are the shaft, the impeller nut, the impeller, the magnets and the CFRP sleeve. The shaft is regarded to be fixed at the locating bearing and axially free at the non locating bearing. For the stiffness of the non-locating bearing in the radial direction a value of $1000 \frac{N}{m}$ is assumed. The values of the first five eigenfrequencies can be found in VII. In figure 24 the mode of the first eigenfrequency is displayed. The first two eigenfrequencies lie below the rotational speed of the pump of 38800 rpm and below 20620 rpm for the fully throttled case. During the start of the pump these eigenfrequencies must be passed through quickly to achieve a stable running pump.

TABLE VII: Eigenfrequencies of the pump

Eigenmodus	Frequency [Hz]	Frequency in [rpm]
1	314	18840
2	330.48	19828.8
3	3642.4	218544
4	3882.3	232938
5	3891.1	233466

IV. DISCUSSION

This section discusses the shortcomings and challenges that were encountered during this study.

- Motor thermal design: The thermal limit was enforced (as a conservative estimate) by limiting the phase current through the winding. Since this method does not address the iron losses or the cryogenic fluids in the vicinity, it may not represent the actual power limits of the motor.
- Cooling channels in the housing are implemented preliminary as placeholders without a detailed sizing.
- No detailed analysis of the gap flow in the drowned rotor sealing concept was conducted. For liquid oxygen, compatibility and ignition may become an issue and should be analyzed in more detail. In general, strict cleanliness regulations should be enforced for all components in a high concentration oxygen environment.
- Only an eigenfrequency analysis of the LOX pump is conducted. The behaviour of the propane pump has not been evaluated. There might exist problems with the eigenfrequencies.
- Battery pack sizing: The battery is currently oversized, due to large margins, mass savings of up to 1.5 kg could be reached if designed on edge.

V. SUMMARY AND OUTLOOK

In this report the preliminary design process of an e-pump is established. Two pumps have been designed, one for LOX and one for propane. For the LOX e-pump a CAD model has been developed and numerous drawings were created. Different challenges in design process were discussed and overcome. However, some uncertainties remain for the detailed development. Some work that remains to be done and should be considered for the future development is listed below.

- Conduct a more detailed eigenfrequency analysis of the LOX and the propane pump.
- Consider further (3D) flow effects for pump design (e.g., volumetric losses, blade blockage) and improve volute design (section IX)
- Conduct physical test to identify the actual bearing loads.
- Efficient motor thermal design can either lead to a simplification (passive cooling sufficient) or a higher power motor (active cooling can transport more waste heat - higher power) enabling extension of the pump operation.
- Detailed LOX ignition analysis.
- Cooling channels in the housing are implemented, but more detailed analysis is needed before manufacturing.
- Battery testing on expected power draw to observe temperature increase over flight.
- Investigate methods for light weight battery cooling for potential mass savings.

VI. TEAM SETUP

• Leonie Büssenschütt

Assembly Design, CAD, Eigenmode Analysis,
Bearing Analysis

• David Stadelbauer

Hydraulic Pump Design and Optimization, CAD

• Sven Steinert

Battery and Power Electronics Design,
Pump Optimization

• Thilo Witzel

Electric Motor Design, CAD

VII. LESSONS LEARNED

A. Soft Skills

- Proper schedule planning is essential.
- Try to parallelize tasks as much as possible.
- Have regular status updates and establish a working routine.
- Establish your own deadlines. Do not try to fix the work until the last moment. At some point accept the results and continue working with that.
- Communication with interfacing teams is crucial.

B. Hard skills

- LOX compatibility with metals is critical.
- Many parameters especially in off-design need to be determined via testing.
- Pump design is a complex process that requires many iterations.

VIII. INDIVIDUAL PART: LEONIE

In this section the bearing calculation shall be discussed in more detail. To obtain a lower limit for the minimum diameter of the bearings, first the shaft shall be considered. It lies at the center of the e-pump and is part of the rotor and links the power unit with the pumping unit. The minimum diameter of the shaft d_w can be calculated with the maximum rotational speed n , the pump power P_p and the allowable shear stress τ_{al} [22].

$$d_w = 3.65 \cdot \sqrt[3]{\frac{P_p}{n \cdot \tau_{al}}} \quad (12)$$

The material of the shaft is DIN St 1.4006. It is selected since it is a standard steel with relative high shear strength and it is also magnetizable which is beneficial for the motor performance [23]. However, there might need to be a coating on the shaft which is compatible with LOX and Propane since the fluids are in direct contact with the shaft. Especially for LOX this is important since it is easily ignitable [24]. The minimum diameters can be found in table VIII.

TABLE VIII: Minimum shaft diameter for LOX and Propane

Pump type	n [rpm]	P_p [W]	τ_{al} [MPa]	d_w [mm]
LOX	38800	1760	370	1.93
Propane	36140	1403	370	1.83

Axial forces The axial forces F_{ax} acting on a pump consist of the momentum force F_I , the unbalanced axial forces F_w and the forces caused by the pressure distributions acting on the impeller shrouds F_{RS} and F_{FS} . For the general case the forces F_{RS} and F_{FS} are assumed to cancel each other such that only $F_{ax} = F_w - F_I$ remains. To calculate the momentum force the density of the fluid ρ , the volume flow rate V and the velocity coefficients c_{1m} and c_{2m} . The streamline deflection angle ϵ is equal to 90° for radial pumps [22].

$$F_I = \rho \cdot V \cdot (c_{1m} - c_{2m} \cdot \cos \epsilon) \quad (13)$$

For the calculation of the unbalanced axial forces the shaft diameter after the impeller d_D , the ambient pressure $p_{amb} = 10^5 \text{ Pa}$ and the static inlet pressure p_1 must be known. This lead to the following equation:

$$F_w = \frac{\pi}{4} \cdot d_D^2 \cdot (p_{amb} - p_1) \quad (14)$$

Radial forces The radial forces F_r of a pump are hard to calculate and are usually determined via experiments. However, there exists an estimation formula to calculate the forces in a rough order of magnitude [22]. The equation consists of the factor $k_{R0} = 0.5$ which is a conservative value at $q^* = 0$, earths gravitational constant g , the pump head H , the outlet diameter d_2 , the total outlet width b_{2tot} , a safety factor for dynamic effects $S_{dyn} = 2$ and the number of stages N_{St} .

$$F_r = k_{R0} \cdot \rho \cdot g \cdot H \cdot d_2 \cdot b_{2tot} \cdot S_{dyn} \cdot N_{St} \quad (15)$$

Bearing dynamic coefficient To calculate the required bearing dynamic coefficient C_{req} the dynamic loading P must be calculated. The general equation is:

$$P = (X \cdot F_r + Y \cdot F_{ax}) \cdot S_{cry} \cdot 10^{-3} \quad (16)$$

TABLE IX: Relevant parameters for the bearing calculation

Pump type	LOX	Propane (stage 2)
ρ [$\frac{\text{kg}}{\text{m}^3}$]	1142	728.53
V [$\frac{\text{m}^3}{\text{s}}$]	0.000565	0.000354
c_{1m} [$\frac{\text{m}}{\text{s}}$]	9.86	9.37
c_{2m} [$\frac{\text{m}}{\text{s}}$]	3.1	3.02
d_D [mm]	7.4	7.4
p_1 [bar]	2.68	17.1
d_2 [mm]	30.7	32.17
b_{2tot} [mm]	5.89	5.16
H [m]	237.5	195.9
N_{St}	1	2
F_I [N]	6.36	2.42
F_w [N]	-7.23	-69.24
F_{ax} [N]	-13.59	-71.66
F_r [N]	481.1	455.39
P [kN]	0.601	0.581
C_{req} [kN]	1.36	1.29

By considering the ratio between radial and axial force it becomes clear that $F_r \gg F_{ax}$ and therefore $X = 0$ and $Y = 1$ [25]. A safety factor $S_{cry} = 1.25$ is assumed to incorporate additional cryogenic effects.

In equation 17 the bearing dynamic coefficient is calculated. p represents the life exponent that is equal to 3 for rolling bearings and L_{10h} is the nominal life in hours which is assumed to be 5.

$$C_{req} = P \cdot \sqrt[p]{\frac{60 \cdot n \cdot L_{10h}}{10^6}} \quad (17)$$

In table IX the values for the parameters and the corresponding forces and coefficients are presented. The whole calculation can also be found in the Phyton code Assembly_Propane.py and Assembly_LOX.py. For the propane pump two main assumptions were made. First, the radial forces can be scaled with the number of stages. Second, only the values for the second stage are used since they lead to higher loads. These initial estimations are made to reach a usable result for the sizing of the bearings. The values should be treated carefully and verified with testing.

Sealing concept To properly seal the pump is one of the main challenges in a turbopump design. For the e-pump a static sealing concept is used. Having a static concept reduces the mechanical losses and also the complexity of the design. The concept can be seen in drawing F. As sealing components standard metal C-rings of type CI-CE are used that can be bought on the market. The three C-rings are assembled in a male-female assembly and the grooves are sized according to [26].

In this sealing concept the bearings are exposed to the fuel or oxidizer. This can lead to multiple problems like sudden ignition or so called "river marks" which are cracks in the balls. To ensure that these effects do not influence the function of the pump or do not appear additional test should be conducted [27].

IX. INDIVIDUAL PART: DAVID

figure 12 illustrates the design process starting with the given input parameters (table II) and preselection of the rotational speed (range) and stage number described in chapter II-D. Subsequently, the input values for each stage are defined, the set of the (kinematic) design variables selected and their values specified, and other (geometric) assumptions such as tip clearances or width ratios could be, theoretically, set for each stage individually. The following stage calculation block iterates over kinematic, thermodynamic and geometric parameters until convergence of η_{hyd} and $\eta_{hyd,R}$ is achieved. Additionally, the deviation of the pressure recovery coefficient of the vaned diffuser from its optimal value (Eq. 23) is minimized by adapting the rotational speed (initially manually but later by means of an optimization). Finally, the overall performance (characteristic) and geometry is evaluated and the stage number adjusted if deemed necessary.

To verify off-design performance for throttled operation all geometric parameters were fixed, and the resulting kinematic and thermodynamic parameters determined iteratively by specifying the partload vaned diffuser pressure recovery coefficient, stator losses and slip factor according to figure 13 in the appendix, and requiring convergence of, again, η_{hyd} and $\eta_{hyd,R}$ but, additionally, the losses in the the vaned diffuser $Z_{H,vaned}$.

The resulting geometries fulfill various feasibility criteria such as (impeller) blade angles within certain ranges (e.g., $60^\circ \leq \beta_{2B} \leq 75^\circ$), minimum tip clearances (≥ 2 mm) between impeller and (vaneless) diffuser and diffuser and volute, minima or maxima for different velocity ratios (e.g., $w_1/w_2 < 1.4$), or quality criteria for the diffuser outlet velocity depending on the meridional inlet velocity or pump head per stage [4]:

$$0.02 < \frac{c_3^2}{2 \cdot g \cdot \Delta H_s} < 0.04 \quad (18)$$

$$0.85 < \frac{c_3}{c_{1m}} < 1.25 \quad (19)$$

The pressure recovery coefficient for the vaneless diffuser can not be theoretically calculated, but an optimal value can be assumed if the area ratio (Eq. 20) is close to its optimum (Eq. 21) depending on an equivalent cross section r_{eq} (Eq. 22) and the diffuser hydraulic length $L_{hyd,vaned}$ [6].

$$A_R = \frac{D_3 \cdot b_3 \cdot \cos(\alpha_3)}{D_{2S} \cdot b_{2S} \cdot \cos(\alpha_{2S})} \quad (20)$$

$$A_{R,opt} = 1.05 + 0.184 \cdot \frac{L_{hyd,vaned}}{r_{eq}} \quad (21)$$

$$r_{eq} = \sqrt{\frac{D_{2S} \cdot \cos(\alpha_{2S}) \cdot b_{2S}}{N_{b,S}}} \quad (22)$$

$$c_{p,opt} = 0.36 \cdot \left(\frac{L_{hyd,vaned}}{r_{eq}} \right)^{0.26} \quad (23)$$

Impeller shock, skin friction and mixing losses were considered according to [4] and assumed to be independent of the flow rate due to recirculation-induced pre-rotation at partload [6]. The incoming flow was assumed to be horizontal ($\alpha_1 = 0$) and homogeneous ($c_{m1} \neq f(r)$), and to further limit the design space, simplify the iterative design process and obtain stages of equal geometry $\Delta H_s = \Delta H/z$ and $c_3 = c_1$ were specified. To avoid high pressure pulsations, noise and vibrations due to non-uniform impeller outlet flow (large blade spacing) $N_{b,R} < 5$ should be avoided if $\Delta H_s > 100$ m, therefore, for impellers with $0.2 < \omega_s < 2$ Gleich [3] recommends 5 to 7 blades ($N_{b,R,P} = N_{b,R,Ox} = 6$). More sophisticated methods to determine appropriate blade numbers are based on the blade loading (see [4]).

The requirements R01 and R02 (minimum number of components and low complexity regarding manufacturing) demand justification for the implementation of diffuser vanes, especially for the single-stage liquid oxygen pump. In the case of volute pumps, the spiral casing not only serves as the pressure boundary of the fluid, but also provides the hydraulic flow path converting velocity into static pressure (diffuser). The (vaneless) diffuser pump configuration was deemed preferable due to [28]:

- higher maximum efficiency and lower efficiency collapse at partload operation
- increased head rise to shut-off (HRTSO) and steeper pump characteristic (higher stability)
- significantly reduced radial loads (more symmetric pressure distribution in volute casing of diffuser pumps) due to less asymmetric volute shape
- decreased pulsations and other unsteady flow phenomena

The stator blade number $N_{b,S,P} = N_{b,S,Ox} = 10$ is selected according to the chosen impeller blade number to limit pressure pulsations and vibrations [4].

The pump volute casing was only roughly sized aiming at low pitch for the spiral (helix) shape and equal cross sections of volute throat and discharge nozzle exit to reduce deceleration, static pressure rise, losses and radial loads (by increased symmetry), ensuring $A_{3Sq} > A_{2Sq}$ as the BEP is specified by the vaned diffuser throat, and considering design recommendations for the cutwater angle and radial tip clearance [6]. Moreover, volute (mainly friction and shock) losses have been neglected and should be subject to further analysis, however, a complete volute casing redesign with the goal of creating a purely symmetric casing is recommended as minimal radial loads and losses could be achieved and, additionally, manufacturing simplified.

X. INDIVIDUAL PART: SVEN

A. Battery Pack design

During the battery pack design, the specific cell characteristics are drawn from data of external tests [29], as they are providing more information than the original data sheet [30]. The external tests covered discharge and charge scenarios under various conditions which fully specify The specific discharge characteristics under different current loads are illustrated in figure 8 and give an impression on the current dependency of losses and overall behaviour. These are the most relevant characteristics of the cells to explain variables during operation, as the change of the energy state provides insight on voltage drops, charge state and heat production of the battery.

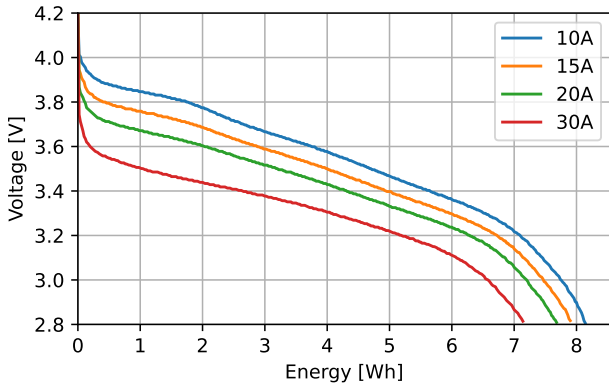


Fig. 8: Discharge curve of the Samsung INR18650-25S cell (data from [29])

B. Pump Optimization

The optimization was carried out with an optimization framework called Optuna [31], which is usually used for hyperparameter optimization of neural networks. This optimizer deploys define-by-run methods where the search space can be dynamically constructed, which is an especially strong optimisation strategy for highly sensitive and non-continuous problems. As the pump design scripts employ a number of checks that need to pass in order to accept the solution as valid, our optimization problem becomes non-continuous as well, which is why this optimizer is a great fit to our problem. The function definition to optimize is held in individual files `pump_design_ox.py` for Oxygen and `pump_design_prop.py` for Propane. The optimization study is defined in `optuna_pump_ox.py` and `optuna_pump_prop.py` accordingly. The investigation range limits for exploration have been iterated to find settings which emerge solutions. The investigated parameter range limits are shown in table X.

TABLE X: Investigated parameter space limits for the optimization study of the pump design

parameter	Oxygen pump	Propane pump
R	0.660 .. 0.678	0.664 .. 0.665
n [rpm]	35000 .. 39001	35000 .. 38001
phi	0.14 .. 0.16	0.145 .. 0.155
psi	0.680 .. 0.701	0.690 .. 0.705

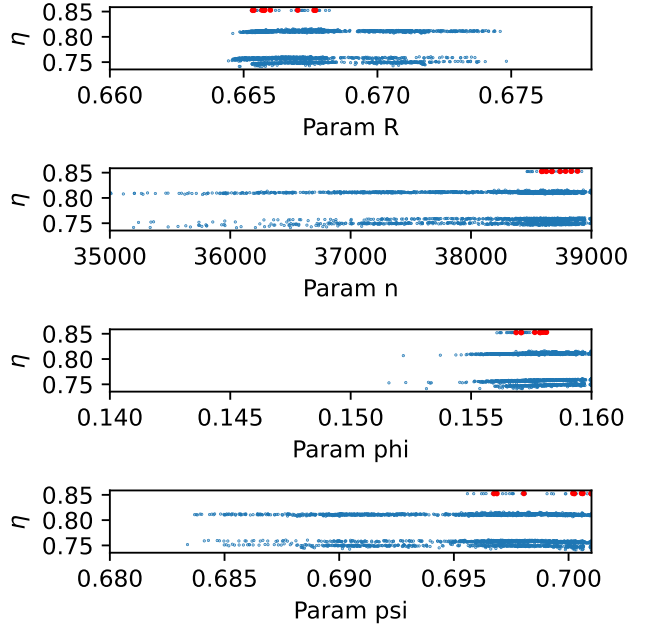


Fig. 9: Optimization results over the investigated range of the Oxygen pump, with the 10 best solution marked in red

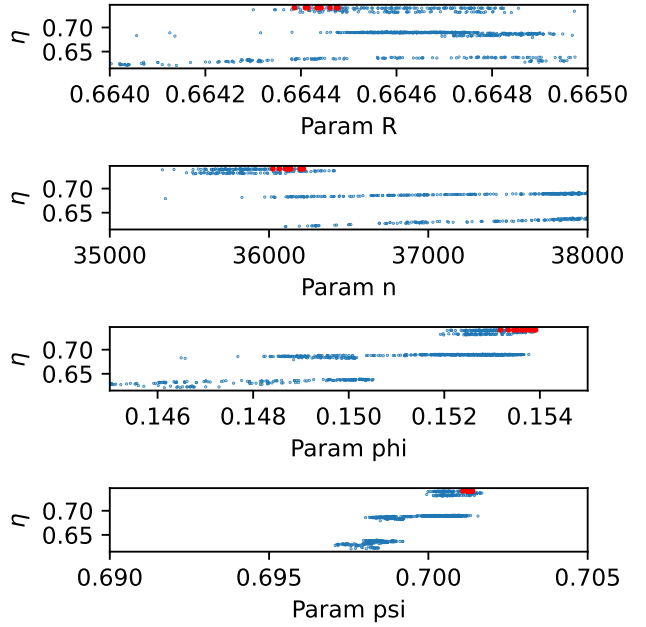


Fig. 10: Optimization results over the investigated range of the Propane pump, with the 10 best solution marked in red

As illustrated in figure 9 and figure 10, all valid solutions are plotted from 16,000 runs. It can be seen that the solution space is highly discretized, which confirms the non-continuous nature of the problem. In all cases the 10 best solutions are clustered and don't collide with the exploration borders, which is why the optimization was concluded as successful.

XI. INDIVIDUAL PART: THILO

A. Electric motor design

For the design of the electric motor, the general approach proposed in [12] is used. The general equation describing the motor power is:

$$P = 2\omega k_w \cos(\phi) \bar{B} \bar{A} \pi r_R^2 l \quad (24)$$

where k_w is the winding factor, \bar{B} [T] is the average radial air gap flux density and \bar{A} [A/m] is the average linear current loading. For a rough design, experience values for the magnetic and current loading can be used (e.g. in [14, p. 299]) depending on the machine type. With analytical approximations, some of these values can be estimated more precisely and geometry parameters can be linked to these characteristic values. For example, the design tool developed for this study uses a Fourier-based 2D analytical magnetic field solution of surface motor permanent magnets [32] to determine \bar{B} and [13, p. 646ff.] to calculate the required magnet thickness. Combined with [15] for the magnet retaining sleeve, the analytical sizing can give a very precise estimate of the rotor geometry. However, since the magnetic flux through the stator is more complex and the motor performance depends heavily on the winding layout of the coils in the stator, the detailed design of the motor is carried out in a commercial FEM tool (Altair Flux), once the analytical estimate produced a sufficient estimate of the motor dimensions.

1) Losses: Two main types of electromagnetic losses occur in motors: **Winding** and **Iron** losses. The losses in the winding originate from the ohmic resistance and can have an AC component for higher-frequency applications (for example: skin effect). The iron losses mainly consist of eddy currents in the conductive ferromagnetic iron parts and the permanent magnets as well as magnetic hysteresis losses due to changing magnetic fields. The iron losses are usually material-specific and depend on the magnetic flux density amplitude and frequency. These losses are modelled in the FEM simulation.

2) Material selection: Because a motor in an aerospace application needs a high gravimetric power density, the high performance electromagnetic steel Vacoflux 50 [33] (approx. 50/50 Iron / Cobalt alloy) is used as stator lamination material. It has two major advantages over common materials: A very high magnetic saturation flux density and a very low specific iron loss.

The rare earth neodymium-based permanent magnet alloy Vacodyn 131 DTP [34] is used because of its high energy density and because this alloy is specifically designed to work in cryogenic temperatures. In fact, the performance of the magnets increases by up to 10 % at 90 K compared to room temperature.

Kapton sheets [35] are used as insulation material between iron and the winding in the stator because it is compatible with cryogenic temperatures.

B. Seal concept verification

The seal concept has two major design criteria that need to be addressed:

- The seal has to withstand the internal pressure of the pump outlet.
- The gap flow between rotor and seal must not introduce significant loss

The **seal ring thickness** can be estimated with Barlow's formula (eqn. 6). To verify this approximation, a 2D axisymmetric FEM calculation is conducted in Solidworks with the final geometry. The maximum operational pressure is set as 32 bar (max pressure of the propane pump). As usual for pressure vessels in space applications, the seal has to withstand proof (1.5 x MEOP) and burst pressure (2.5 x MEOP).

To prevent excessive eddy current losses in the sleeve due to the changing magnetic field, the sleeve material should not be conductive. PEEK is chosen as seal sleeve material because it is a chemically inert, has good mechanical properties and is fire resistant [36]. figure 17 depicts the factor of safety results (calculated with properties in table XI) for the burst pressure case showing positive margins (> 1) in the entire part.

The **viscous losses** in two concentric rotating cylinders are a problem that has been experimentally analyzed extensively and can be calculated with a torque coefficient:

$$C_m(Re, Ta, \delta, r_R) = \frac{2M}{\pi \cdot \rho \cdot \omega^2 \cdot r_R^4 \cdot l} \quad (25)$$

$$P = M \cdot \omega \quad (26)$$

where M is the friction torque, ρ is the fluid density, ω is the angular velocity, r_R is the rotor radius, δ is the gap width (radial clearance) and l is the motor length. The moment coefficient C_m can be determined using empirical relations depending on the geometry, Reynolds ($\rho \omega r_R \delta / \mu$) number and Taylor ($Re \sqrt{\delta / r_R}$) number. Different correlations exist for the linear, transition and turbulent regimes as described in [37]. These correlations have been successfully applied to air gap drag in electric motors in [38]. These equations allow to estimate the drag losses in the air gap depending on the rotational speed and fluid. The results are depicted in figure 18. They are well below 1 W and can be neglected for the design of the pump. Nevertheless, the flow in the gap including heat generation and ignition hazard of the assembly should be investigated in more detail in the future.

TABLE XI: PEEK Material parameters [39]

Variable	Value	Unit
ρ	1320	kg/m ³
σ_{max}	96.5	MPa
E	3380	MPa

REFERENCES

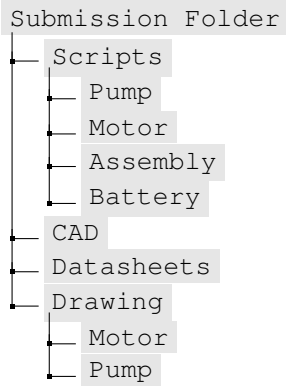
- [1] Juyeon Lee et al. "Performance analysis and mass estimation of a small-sized liquid rocket engine with electric-pump cycle". In: *International Journal of Aeronautical and Space Sciences* 22 (2021), pp. 94–107.
- [2] Alexander L Aueron and L Dale Thomas. "An Assessment of Electric Pump Fed Nuclear Thermal Propulsion". In: *AIAA SCITECH 2022 Forum*. 2022, p. 0794.
- [3] Jimin Xu et al. "An overview of bearing candidates for the next generation of reusable liquid rocket turbopumps". In: *Chinese Journal of Mechanical Engineering* 33 (2020), pp. 1–13.
- [4] Marco Gambini and Michela Vellini. *Turbomachinery - Fundamentals, Selection and Preliminary Design*. Springer Cham, 2021.
- [5] Johann F. Gülich. "Bemerkungen zur Kennlinienstabilität von Kreiselpumpen". In: *Pumpentagung Karlsruhe*. 1988.
- [6] Johann F. Gülich. *Centrifugal Pumps*. Springer-Verlag Berlin, 2010.
- [7] Joseph P. Veres. *Centrifugal and Axial Pump Design and Off-Design Performance Prediction*. Tech. rep. 1994.
- [8] Ronald W. Humble, Gary N. Henry, and Wiley J. Larson. *Space Propulsion Analysis and Design*. United States Department of Defense, NASA, 1995.
- [9] Kosuke Toyama, Peter W. Runstadler Jr., and Robert C. Dean Jr. "An Experimental Study of Surge in Centrifugal Compressors". In: (1977).
- [10] Merve Yıldırım, Mehmet Polat, and Hasan Kürüm. "A survey on comparison of electric motor types and drives used for electric vehicles". In: *2014 16th International Power Electronics and Motion Control Conference and Exposition*. 2014, pp. 218–223. DOI: 10.1109/EPEEMC.2014.6980715.
- [11] D. Alban, L. Brenner, and D. Gerling. "Five-Phase Electric Motor Design for Light Sport Aeroplane". en. In: (2023). DOI: 10 . 25967 / 610390. URL: [https://publikationen.dgler.de/?tx_dglrpublications_pi1\[document_id\]=610390](https://publikationen.dgler.de/?tx_dglrpublications_pi1[document_id]=610390).
- [12] S. MEZANI et al. "Sizing Electrical Machines Using OpenOffice Calc". In: (2022). DOI: 10 . 13009 / EUCASS2022-6110. URL: <https://www.eucass.eu/doi/EUCASS2022-6110.pdf>.
- [13] Ekkehard Bolte. *Elektrische Maschinen*. Springer Berlin Heidelberg, 2012. ISBN: 9783642054853. DOI: 10.1007/978-3-642-05485-3. URL: <http://dx.doi.org/10.1007/978-3-642-05485-3>.
- [14] Juha Pyrhönen, Tapani Jokinen, and Valéria Hrabovcová. *Design of Rotating Electrical Machines*. Wiley, Oct. 2013. ISBN: 9781118701591. DOI: 10 . 1002 / 9781118701591. URL: <http://dx.doi.org/10.1002/9781118701591>.
- [15] A. Binder, T. Schneider, and M. Klohr. "Fixation of buried and surface mounted magnets in high-speed permanent magnet synchronous motors". In: *Fourth IAS Annual Meeting. Conference Record of the 2005 Industry Applications Conference, 2005*. IEEE, 2005. DOI: 10.1109/ias.2005.1518863. URL: <http://dx.doi.org/10.1109/IAS.2005.1518863>.
- [16] Gerhard Knappstein. *Statik, insbesondere Schnittprinzip*. Harri Deutsch Verlag, 2007.
- [17] Low Voltage HBC Motor Controller - MGM-COMPRO. 2024. URL: <https://www.mgm-compro.com/brushless-motor-controllers/up-to-6-kw-motor-controllers/> (visited on 03/03/2024).
- [18] JIABAIDA 10S-17S 80A - Battery Management System. 2024. URL: <https://jiabaidabms.com/products/jbd-smart-bms-10s-17s-60v-40a-60a-80a-lithium-battery-pcb-with-ntc-ports?variant=42062222360738> (visited on 03/03/2024).
- [19] Gehrig. *HYSN-Hybridkugellager / HYSN-Hybrid ball bearing*. Sand am Main, Germany.
- [20] O-, X- und Tandem Anordnung. URL: <https://waelzlagerwissen.de/gestaltung-lagerung/o-x-und-tandem-anordnung/> (visited on 03/16/2024).
- [21] Gehrig. *HYSN 7xxx T3 Serie / HYSN 7xxx T3 series*. Sand am Main, Germany.
- [22] Johann Friedrich Gülich. *Kreiselpumpen: ein Handbuch für Entwicklung, Anlagenplanung und Betrieb*. Springer-Verlag, 2013.
- [23] EN 1.4006 (X12Cr13) Stainless Steel. URL: <https://www.makeitfrom.com/material-properties/EN-1.4006-X12Cr13-Stainless-Steel> (visited on 02/10/2024).
- [24] Jean-Luc Bozet et al. "Liquid oxygen compatibility of materials for space propulsion needs". In: *4th European Conference for Aerospace Sciences (EUCASS)*. 2011.
- [25] Hermann Roloff. *Maschinenelemente: Normung, Berechnung, Gestaltung*. Springer-Verlag, 2013.
- [26] High Tech Metal Seals. *Resilient Metal Seals - Product Guide*. Mechelen, Belgium.
- [27] HG Gibson. *Design Guide for Bearings Used in Cryogenic Turbopumps and Test Rigs*. Tech. rep. 2019.
- [28] Rodleta. *Explanation diffuser pump advantages over volute pumps*. URL: <https://www.rodelta.com/explanation-diffuser-pumps/> (visited on 03/02/2024).
- [29] Test of Samsung INR18650-25S 2500mAh (Purple) - lygte-info.dk. 2024. URL: <https://lygte-info.dk/review/batteries2012/Samsung%20INR18650-25S%202500mAh%20%28Purple%29%20UK.html> (visited on 03/03/2024).
- [30] Specification of Product No. INR18650-25S Version 1.1 - SAMSUNG SDI Co., Lt. URL: https://bestbattery.com.ua/image/catalog/Batteries/Samsung_Li-ion/Samsung_INR18650_25S/Samsung_25S_2500_datasheet.pdf (visited on 02/10/2024).
- [31] Takuya Akiba et al. "Optuna: A Next-generation Hyperparameter Optimization Framework". In: *Proceedings of the 25th ACM SIGKDD International Conference on Knowledge Discovery and Data Mining*. 2019.

- [32] Z. Q. Zhu et al. “Instantaneous magnetic field distribution in brushless permanent magnet DC motors. I. Open-circuit field”. In: *IEEE Transactions on Magnetics* 29 (1993), pp. 124–135. URL: <https://api.semanticscholar.org/CorpusID:122823460>.
- [33] VACODYM 131 TP / VACODYM 131 DTP für Tieftemperaturanwendungen. URL: https://vacuumschmelze.com/03_Documents/Brochures/Cobalt-Iron%20Alloys.pdf (visited on 03/19/2024).
- [34] VACODYM 131 TP / VACODYM 131 DTP für Tieftemperaturanwendungen. URL: https://vacuumschmelze.com/03_Documents/Brochures/Vacodynam_131_de.pdf (visited on 03/19/2024).
- [35] DuPont Kapton. URL: <https://www.dupont.com/content/dam/dupont/amer/us/en/ei-transformation/public/documents/en/EI-10167-Kapton-General-Specifications.pdf> (visited on 03/19/2024).
- [36] Aditya Ramgobin, Gaëlle Fontaine, and Serge Bourbigot. “Thermal Degradation and Fire Behavior of High Performance Polymers”. In: *Polymer Reviews* 59.1 (Jan. 2019), pp. 55–123. ISSN: 1558-3716. DOI: 10.1080/15583724.2018.1546736. URL: <http://dx.doi.org/10.1080/15583724.2018.1546736>.
- [37] E. Bilgen and R. Boulos. “Functional Dependence of Torque Coefficient of Coaxial Cylinders on Gap Width and Reynolds Numbers”. In: *Journal of Fluids Engineering* 95.1 (Mar. 1973), pp. 122–126. ISSN: 1528-901X. DOI: 10.1115/1.3446944. URL: <http://dx.doi.org/10.1115/1.3446944>.
- [38] Xiaoyan Huang et al. “Design of a Five-Phase Brushless DC Motor for a Safety Critical Aerospace Application”. In: *IEEE Transactions on Industrial Electronics* 59.9 (Sept. 2012), pp. 3532–3541. ISSN: 1557-9948. DOI: 10.1109/tie.2011.2172170. URL: <http://dx.doi.org/10.1109/TIE.2011.2172170>.
- [39] About PEEK. URL: <https://www.curbellplastics.com/materials/plastics/peek/>.

APPENDIX

A. Digital Appendix

This is the general folder structure of the digital appendix. The digital appendix is available [online](#) or in the .zip file attached to this report. The folder *Scripts* holds all the design tools and calculation documents that were used for the design of the individual pump components. The folder *CAD* holds all relevant Solidworks files for the CAD model of the pump. The relevant assemblies are the the LOX Pump (LOX-Pump.SLDASM) and the battery including the controllers (ElectricAssy.SLDASM). In *Datasheets*, all relevant datasheets for bought components of the pump are stored. The *Drawing* folder contains the assembly drawing of the entire pump and the single parts that make up the electric motor.



In general, the appendix presents additional figures and tables that may be helpful for the reader to understand the content presented in the main report. If they are helpful to illustrate certain results, the appendix content is referenced accordingly in the main text section. However, they are not strictly necessary to understand the content of the main report.

B. Trade Space Exploration

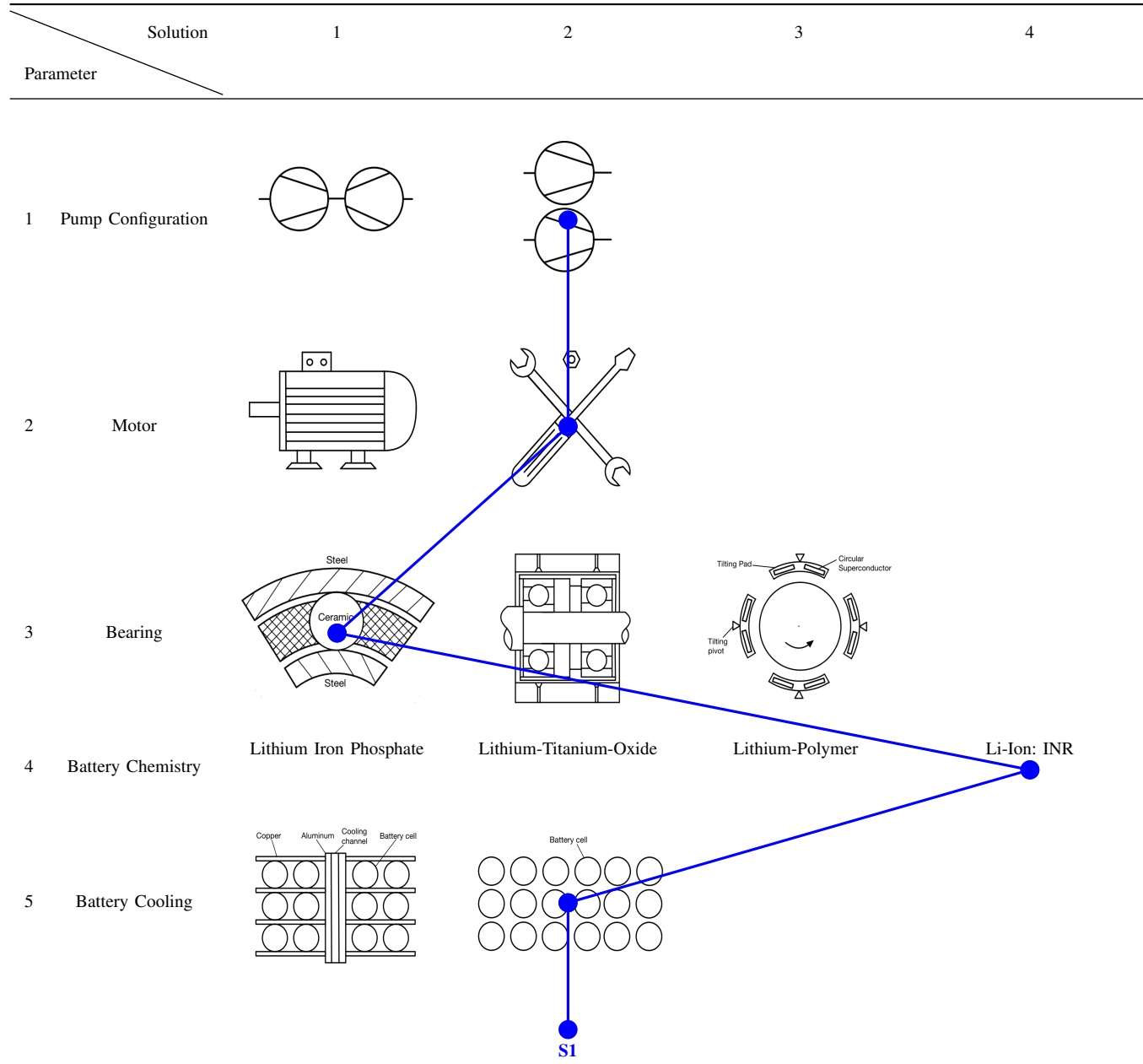


TABLE XII: Morphological Box

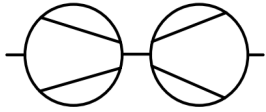
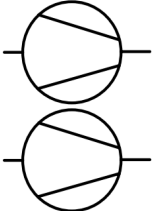
Structure	Advantages	Disadvantages
1  Combined Pumps	<ul style="list-style-type: none"> Possibly lighter & more compact Motor, shaft and bearings only needed once 	<ul style="list-style-type: none"> Sealing more complicated Circuits not independently controllable Worse overall efficiency Inflexible development & enhancements Low adaptability to other designs
2  Separate Pumps	<ul style="list-style-type: none"> Better individual performance Easier sealing design Suitable for general purpose Easier development & enhancements Separately controllable 	<ul style="list-style-type: none"> Probably heavier & larger Motor, shaft and bearings need repeatedly

TABLE XIII: Possible Pump Configurations

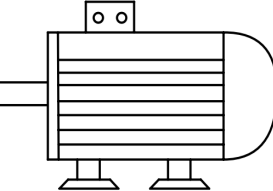
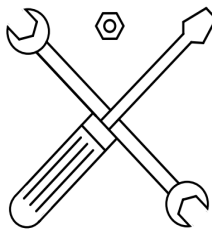
Structure	Advantages	Disadvantages
1  Buy motor	<ul style="list-style-type: none"> Lower cost if mass-produced standard model fits the needs of the pump Lower engineering effort and risk Potentially shorter lead times 	<ul style="list-style-type: none"> Low flexibility and limited possibility of integration into the pump system design (most commercial motors are already integrated into a housing with bearings, cooling, etc.) Larger and heavier (e.g. cooling with cryogenic media not incorporated into the design, thermal considerations are the limiting factor for power density) No standard motors fit the specific requirements of the pump (very high speeds, cryogenic operation)
2  Design Motor	<ul style="list-style-type: none"> High design flexibility Performance can be optimized for required design points Very efficient integration into the pump system (geometry, cooling, power supply requirements, etc.) Specific requirements such as cryogenic compatibility require non-standard materials and manufacturing 	<ul style="list-style-type: none"> Additional engineering effort for electrical and mechanical design of the machine Higher development risk compared to buying a machine Potentially higher costs (low-volume prototype manufacturing vs. a mass-produced bought machine)

TABLE XIV: Make or buy decision electric motor

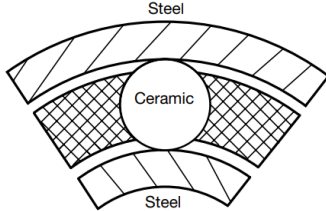
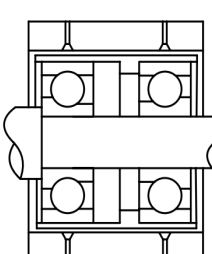
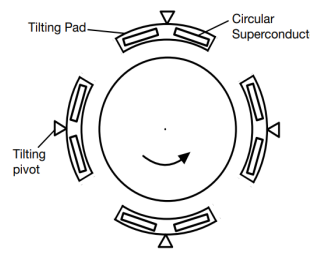
Structure	Advantages	Disadvantages
1  Ceramic Bearing	<ul style="list-style-type: none"> • Well established (TRL9) • Profound knowledge base • Possibly accessible for acquisition → low development effort 	<ul style="list-style-type: none"> • Lossy • Limits in rotational speed • Low reusability
2  Hybrid Bearing	<ul style="list-style-type: none"> • Better reusability • Higher rotational speeds • Less lossy 	<ul style="list-style-type: none"> • Limited Experience (TRL5-6) • Not flight proven • Not easily purchasable
3  Superconducting Magnetic Bearing	<ul style="list-style-type: none"> • Possibly least lossy • Possibly highest reusability • High research value 	<ul style="list-style-type: none"> • Least Experience (TRL3-4) • Highest development effort • Not purchasable

TABLE XV: Bearing Options

Structure	Advantages	Disadvantages
1 Lithium Iron Phosphate (LiFePO4)	<ul style="list-style-type: none"> • Safest • Longest cycle life • High thermal stability • Lowest Cost 	<ul style="list-style-type: none"> • Moderate energy density • Moderate power density
2 Lithium-Titanium-Oxide (LTO)	<ul style="list-style-type: none"> • Highest power density • Fastest charge rate • Lowest self-discharge rate 	<ul style="list-style-type: none"> • Lowest energy density • Hardly accessible • More expensive
3 Lithium-Polymer (LiPo)	<ul style="list-style-type: none"> • Higher power density • Most flexible in shape and size 	<ul style="list-style-type: none"> • Lower energy density • Shortest cycle life
4 Li-Ion: INR (LiNiMnCoO2)	<ul style="list-style-type: none"> • Big range in power density • Widely available • Vast amount of product variants to choose from 	<ul style="list-style-type: none"> • Lower energy density

TABLE XVI: Possible Battery Chemistry

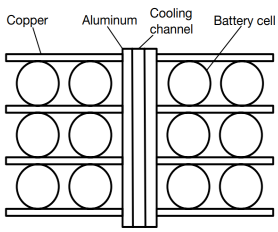
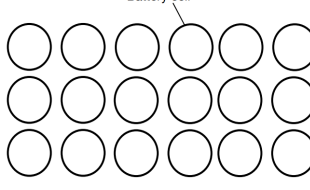
Structure		Advantages	Disadvantages
1	 Battery with active Cooling	<ul style="list-style-type: none"> • Lower system mass achievable 	<ul style="list-style-type: none"> • Adds complexity • Needs to be actively regulated • Narrow temperature window
2	 Battery without active Cooling	<ul style="list-style-type: none"> • Simple setup • Increased cell life • Bigger energy budget 	<ul style="list-style-type: none"> • Increased system mass by approx. 1/3

TABLE XVII: Battery Cooling Tradeoff

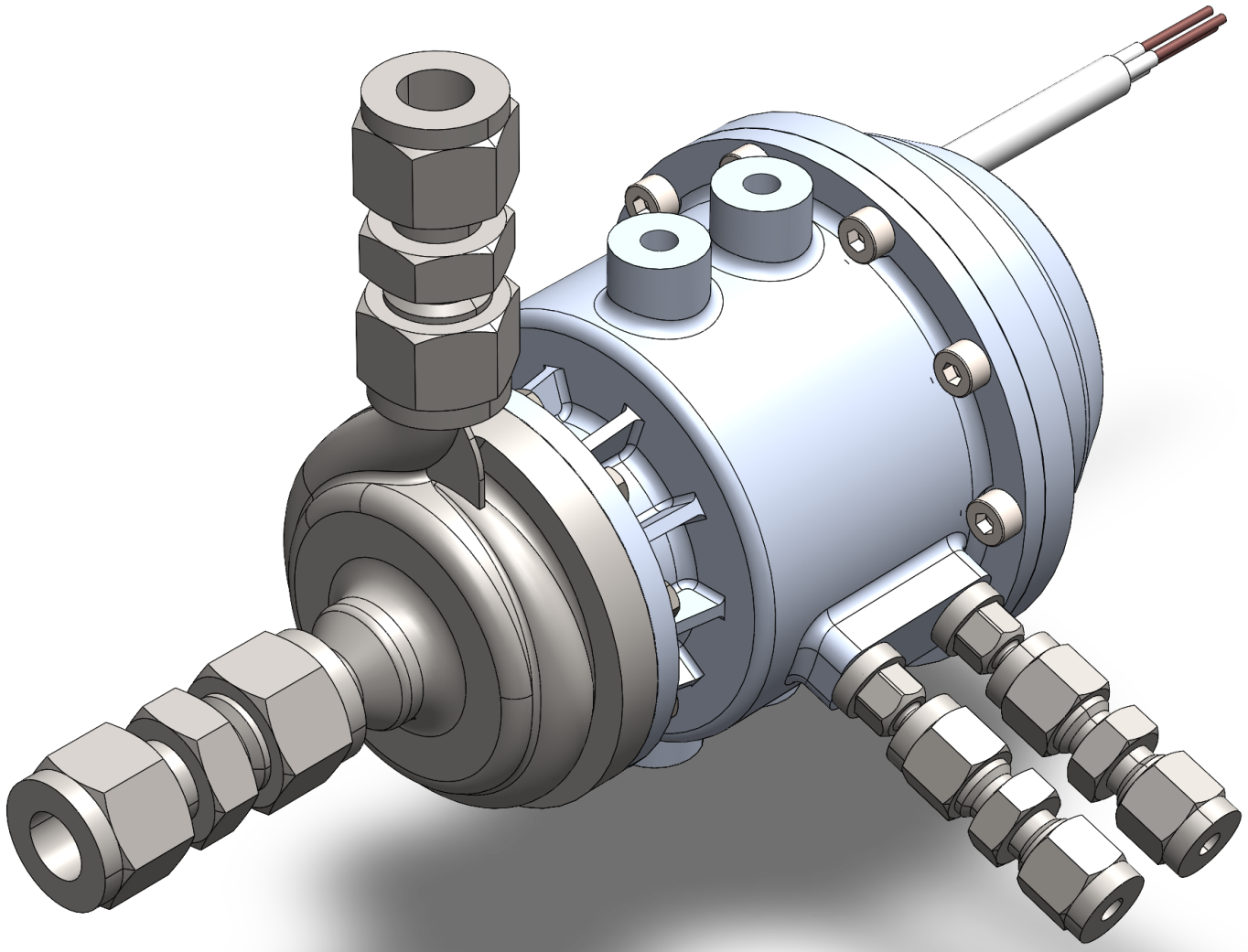


Fig. 11: CAD rendering of the LOX Pump

C. Pump

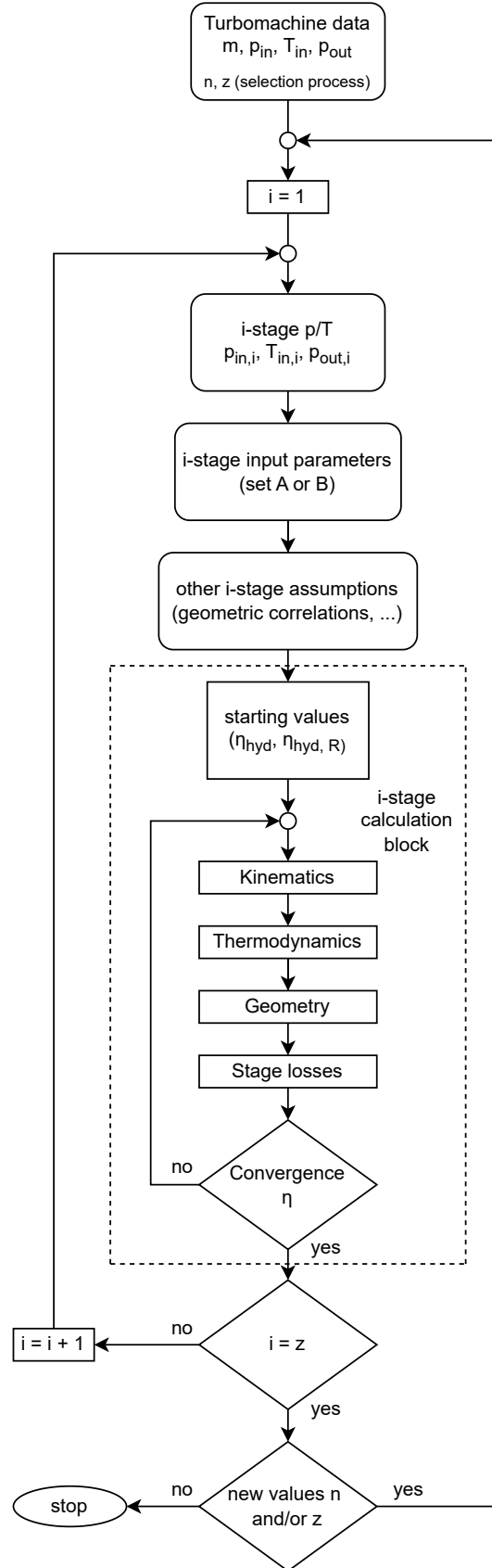


Fig. 12: Flowchart of the pump impeller and diffuser design process

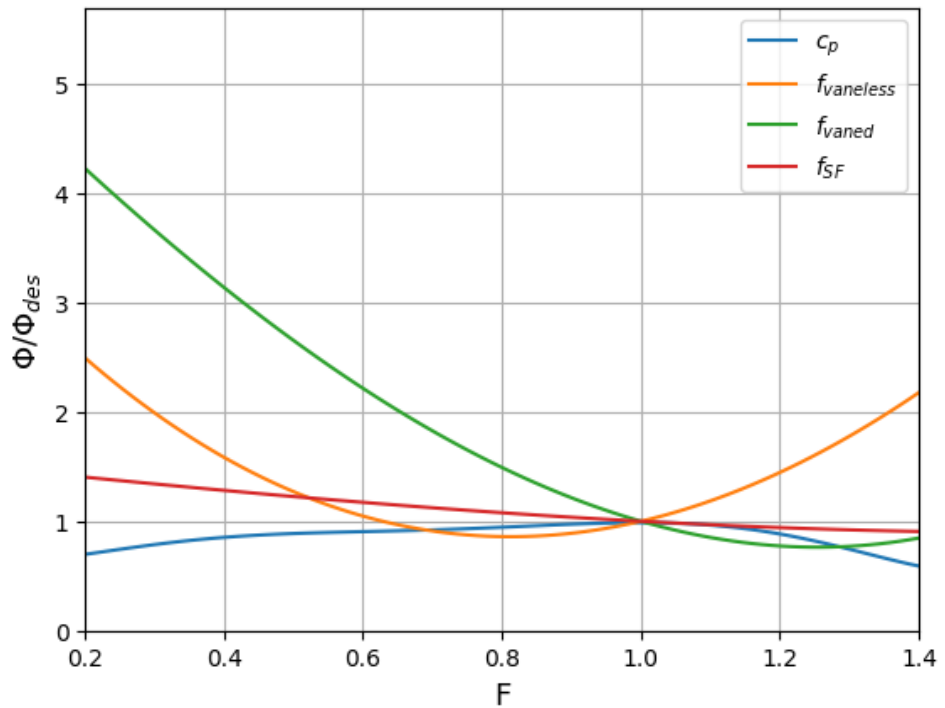


Fig. 13: Scaling functions for diffuser losses, vaneless diffuser pressure recovery coefficient and slip factor at off-design

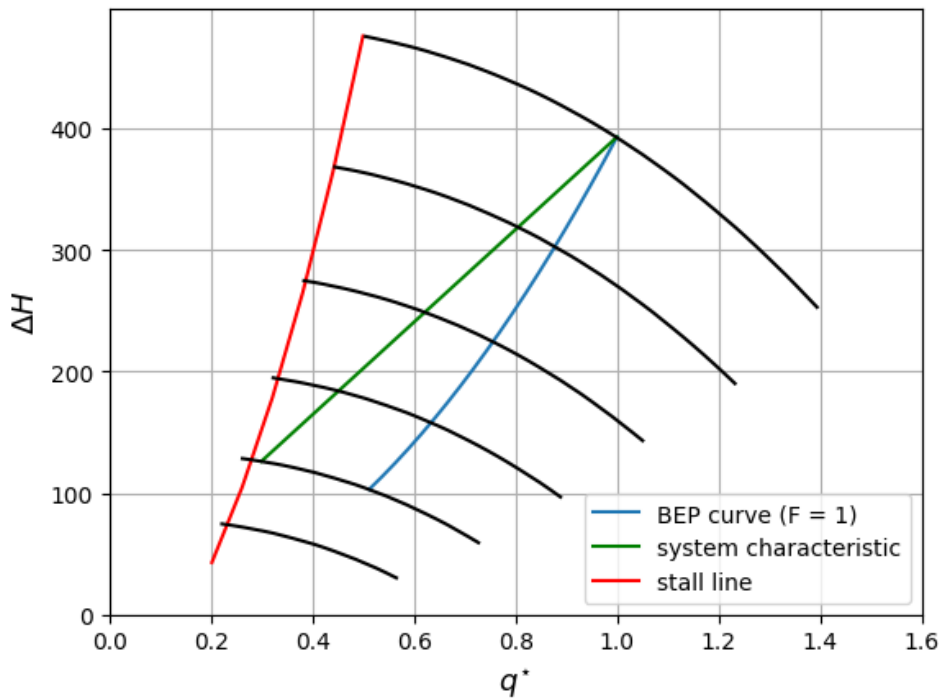


Fig. 14: Propane pump performance map

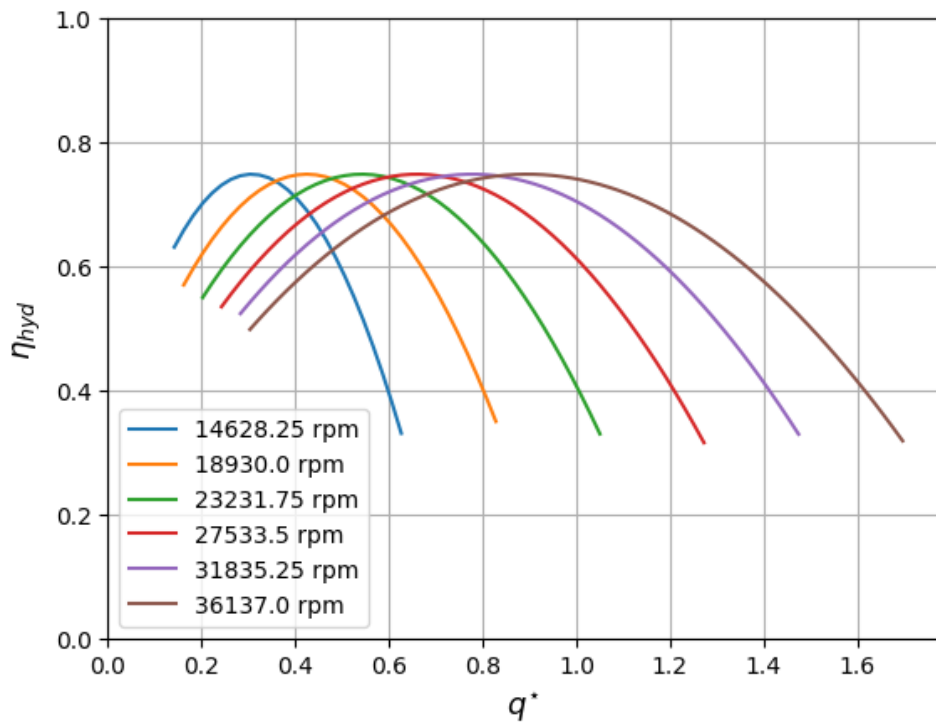


Fig. 15: Propane pump hydraulic efficiencies for different rotational speeds

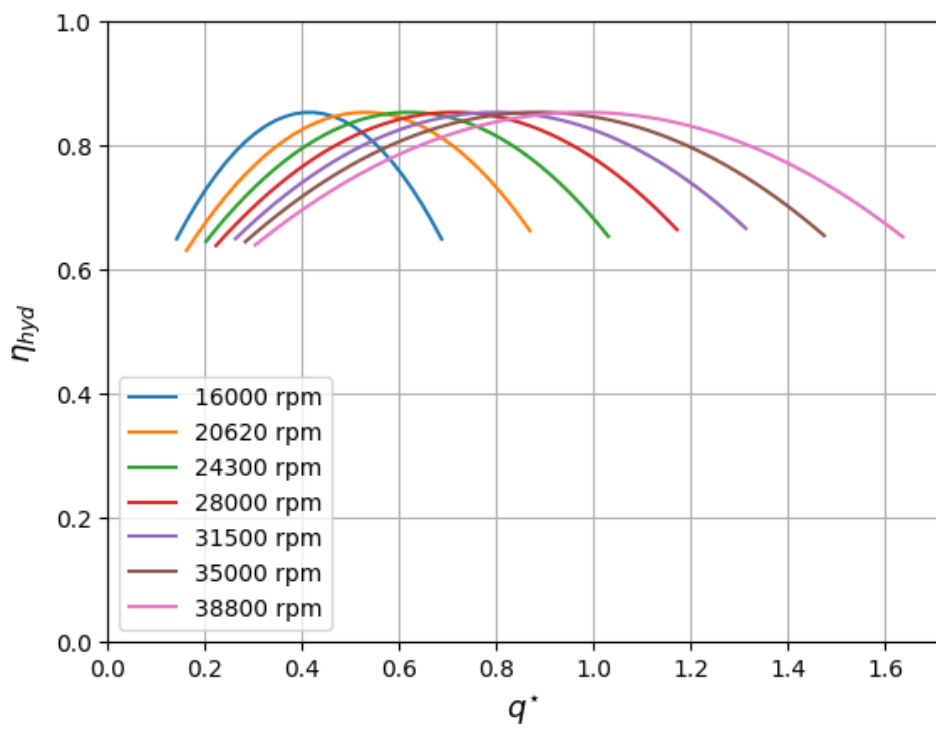


Fig. 16: Oxygen pump hydraulic efficiencies for different rotational speeds

TABLE XVIII: Pump parameter overview

	Parameter name	Symbol	Oxygen pump		Propane pump				Unit
Operating point	Volume flow fraction	q^*	0.3	1	0.3		1		-
Stage	Stage number	z	1	1	1	2	1	2	-
Geometry	Impeller inlet tip diameter	D_{1t}	11.4				10.6		mm
	Impeller inlet hub diameter	D_{1h}	7.7				8		mm
	Impeller outlet diamter	D_2	30.7				32.2		mm
	Vaned diffuser inlet diameter	D_{2S}	35.7				37.5		mm
	(Vaned) diffuser outlet diameter	D_3	38.5				39.5		mm
	Impeller hydraulic diameter	$D_{hyd,R}$	2.35				1.75		mm
	Vaned diffuser hydraulic diameter	$D_{hyd,vaned}$	1.76				1.36		mm
	Impeller inlet width	b_1	1.9				1.29		mm
	Impeller outlet width	b_2	1.89				1.16		mm
	Vaned diffuser inlet width	b_{2S}	2.08				1.28		mm
	(Vaned) diffuser outlet width	b_3	2.08				1.28		mm
	Impeller outlet blade distance	O_2	4.33				4.56		mm
	Vaned diffuser inlet blade distance (throat)	O_{2S}	0.79				0.73		mm
	Impeller hydraulic length	$L_{hyd,R}$	29.1				30.7		mm
	Vaneless diffuser hydraulic length	$L_{hyd,vaneless}$	2.5				2.5		mm
	Vaned diffuser hydraulic length	$L_{hyd,vaned}$	9.2				7.9		mm
	Impeller outlet blade angle	β_{2B}	74.4				74.3		deg
Kinematics	Equivalent cross section	r_{eq}	0.72				0.54		mm
	Vaned diffuser area ratio	A_R	3.51				4.07		-
	Vaned diffuser optimal area ratio	$A_{R,opt}$	3.4				3.73		-
	Impeller outlet absolute flow angle	α_2	88.3	85.9	87.7		86		deg
	Impeller inlet relative flow angle	β_1	77.1	67.1	72.2		65		deg
	Impeller outlet relative flow angle	β_2	84.9	80.6	83.5		80.6		deg
	Impeller inlet absolute velocity	c_1	2.84	9.86	3.37		9.37		m/s
	Impeller inlet absolute meridional velocity	c_{1m}	2.84	9.86	3.37		9.37		m/s
	Impeller inlet absolute tangential velocity	c_{1u}	0	0	0		0		m/s
	Impeller inlet (tip) circumferential velocity	u_1	12.4	23.3	10.5		20.1		m/s
Thermodynamics	Impeller inlet (tip) relative velocity	w_1	12.7	25.3	11.1		22.2		m/s
	Impeller inlet (tip) tangential velocity	w_{1u}	12.4	23.3	10.5		20.1		m/s
	Average velocity at impeller throat area	w_{1q}	10.7	21.8	9.8		20		m/s
	Impeller inlet mean relative velocity	w_{1M}	10.7	21.8	9.8		20		m/s
	Impeller mean relative velocity	\bar{w}_R	5.1	15.1	5.7		14.3		m/s
	Impeller outlet absolute velocity	c_2	30.7	43.8	27		42.8		m/s
	Impeller outlet absolute meridional velocity	c_{2m}	0.89	3.1	1.1		3		m/s
	Impeller outlet absolute tangential velocity	c_{2u}	27.3	43.7	26.1		42.7		m/s
	Impeller outlet circumferential velocity	u_2	33.1	62.4	31.9		60.9		m/s
	Impeller outlet relative velocity	w_2	10	18.9	9.6		18.4		m/s
	Impeller outlet relative tangential velocity	w_{2u}	9.9	18.7	9.5		18.2		m/s
	Vaneless diffuser mean relative velocity	$\bar{w}_{vaneless}$	5	17.3	6.2		17.3		m/s
	Vaned diffuser inlet absolute velocity	c_{2S}	23.5	34.6	22.6		38.1		m/s
	Vaned diffuser inlet absolute tangential velocity	c_{2Su}	23.5	34.5	22.6		38		m/s
	Vaned diffuser inlet absolute meridional velocity	c_{2Sm}	0.7	2.4	0.86		2.4		m/s
	Vaned diffuser throat absolute velocity	c_{2Sq}	10	34.6	13.7		38.1		m/s
	(Vaned) diffuser absolute outlet velocity	c_3	2.84	9.86	3.37		9.37		m/s
	Viscosity at impeller inlet	μ_1	0.000196	0.000196	0.00747		0.00755		Pa s
	Viscosity at vaned diffuser inlet	μ_{2S}	0.000195	0.000195	0.00734		0.0072		Pa s
Thermodynamics	Impeller inlet static pressure	p_1	3.25	2.68	3.26	7.8	3.05	17.1	bar
	Impeller outlet static pressure	p_2	8.8	22.7	6.5	11	15.4	29	bar
	Vaned diffuser inlet static pressure	p_{2S}	10.3	24.4	6.4	11	12.1	27.1	bar
	(Vaned) diffuser outlet static pressure	p_3	12.3	29.3	7.8	12.3	17.1	31.2	bar
	Vaneless diffuser losses	$Z_{H,vaneless}$	6.8	20.6	11.4		44.9		m
	Vaned diffuser losses	$Z_{H,vaned}$	9.8	14.1	7		13.7		m
	Stator losses	$Z_{H,S}$	16.6	34.7	18.4		58.5		m
	Impeller skin friction and mixing losses	$Z_{H,sf}$	-	6.1	-		10.1		m
	Impeller shock losses	$Z_{H,shock}$	-	0	-		0		m
	Rotor losses	$Z_{H,R}$	1.73	6.1	2.76		10.1		m
	Pump losses	Z_H	18.3	40.8	21.1		68.6		m
	Specific work	W	770	2726	713		2598		J/kg
	Power	P	143	1760	66		748		W
	Hydraulic pump efficiency	η_{hyd}	76.6	85.3	70.9		74.1		%
	Hydraulic rotor efficiency	$\eta_{hyd,R}$	96.7	96.7	94.3		94.3		%

D. Electric Motor

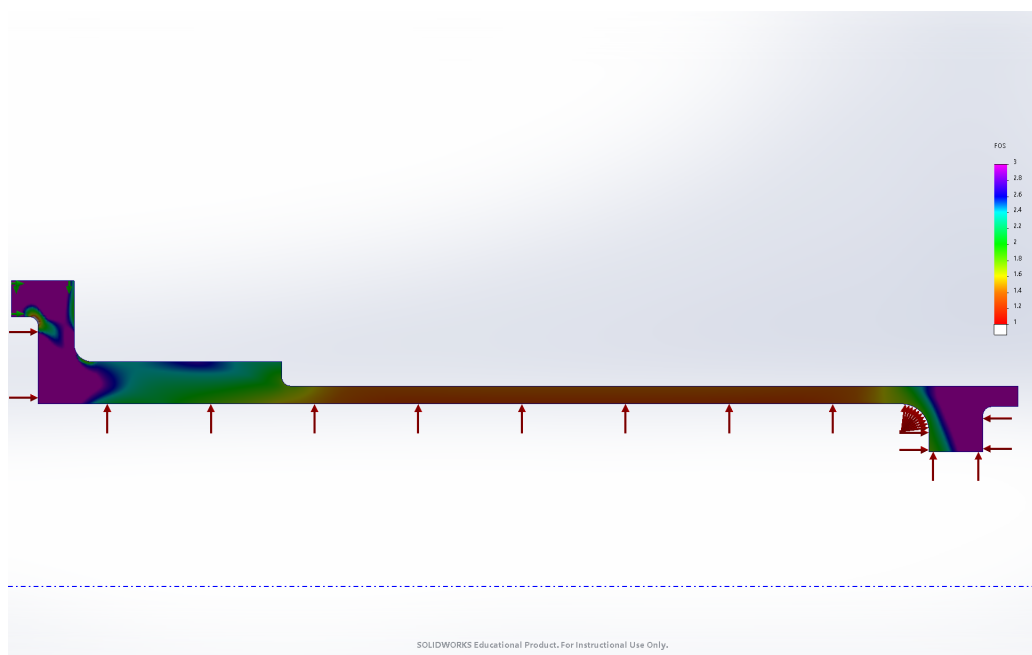


Fig. 17: Factor of safety ($\sigma_{allowed}/\sigma$) for 80 bar (2.5 x MEOP) internal pressure

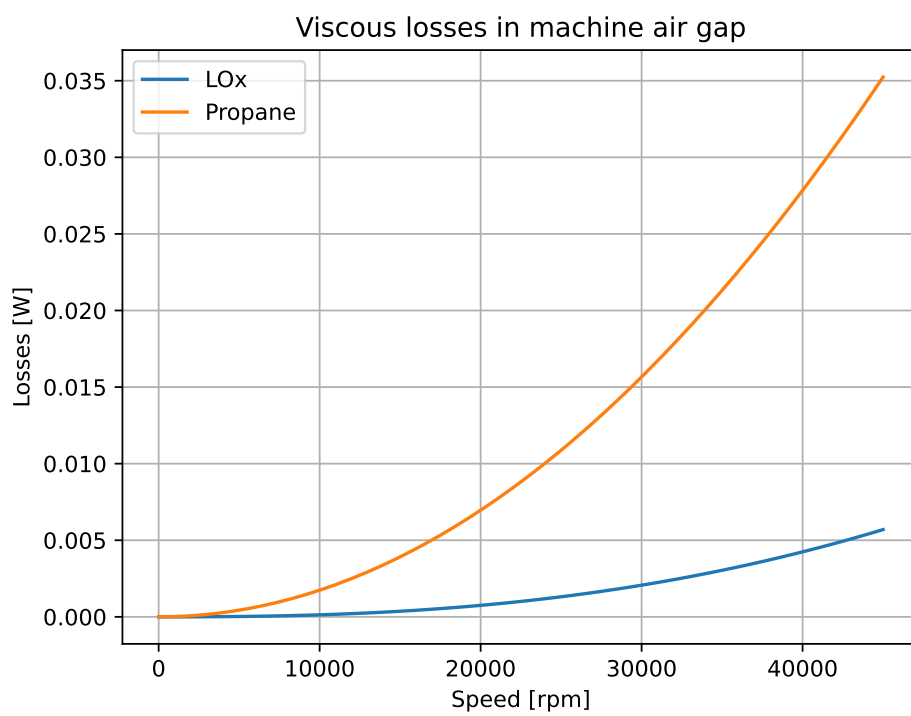


Fig. 18: Friction losses in the air gap calculated acc. to [37]

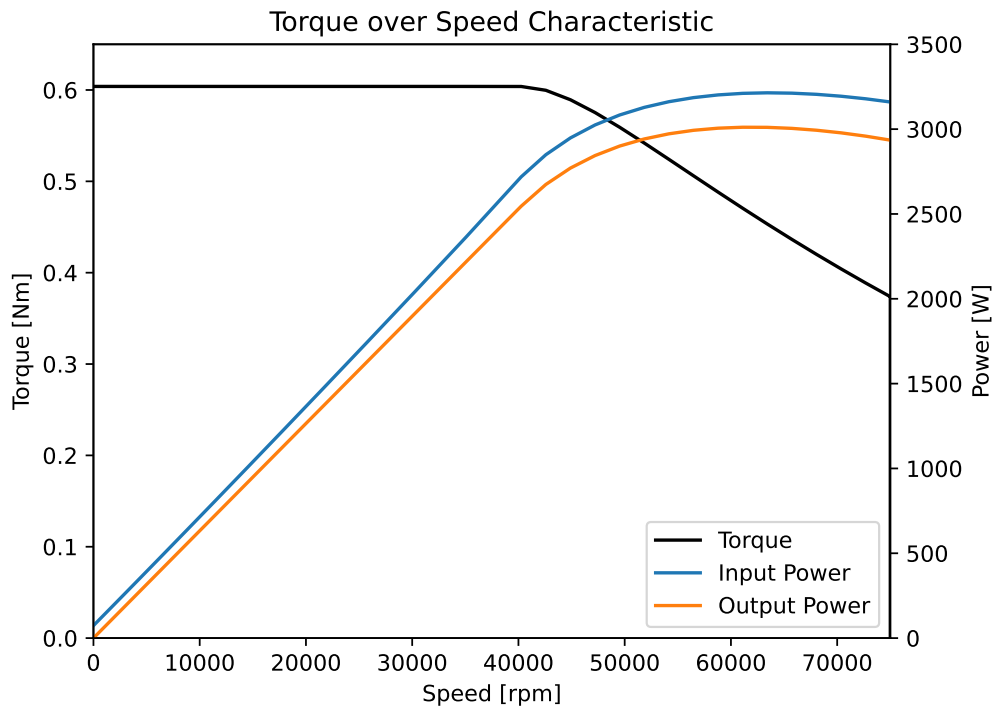


Fig. 19: Calculated torque and power characteristic at maximum allowed current.

TABLE XIX: Motor output parameters

Variable	Value	Unit
Load Point Torque	0.61	Nm
Load Point Speed	38000	rpm
Load Point Power	2445	W
Load Point Efficiency	94.1	%
Phase Current	61.85	Arms
Phase-Phase Voltage	28.9	Vrms
Outer Diameter	57	mm
Inner Diameter	10	mm
Length	30	mm
Pressure seal thickness	0.8	mm
Rotor sleeve thickness	0.2	mm
CAD mass	0.627	kg
Pole pairs	2	-

E. Battery Pack

TABLE XX: Parts list of the electric assembly and mass budget

description	m [g]	pc.	m [kg]
Samsung INR18650-25S	47	84	3.948
18650 Spacer	0.5	84	0.042
Nickel Strip	0.4	84	0.034
BMS JBD 10S-17S 80A	100	3	0.300
BLDC driver HBCi10063	63	2	0.126
Sum			4.450
margin			20%
Total			5.340

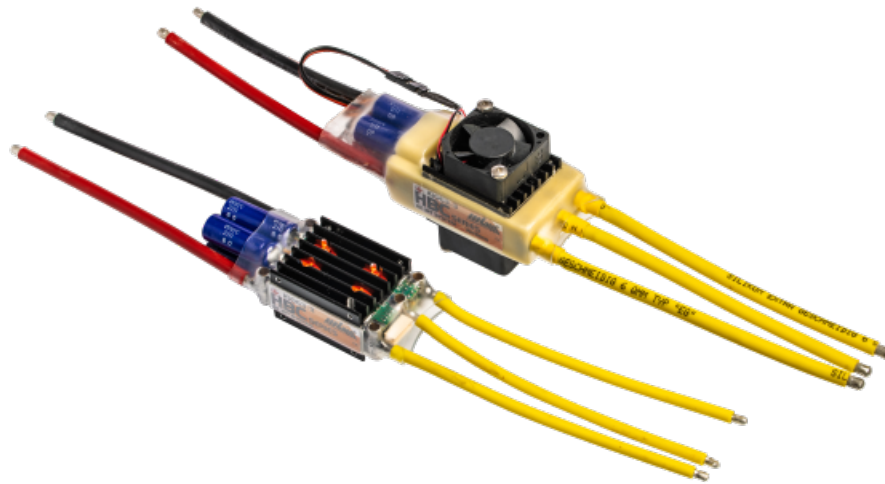


Fig. 20: Product photo of the MGM-COMPRO 6kW Low Voltage HBC Motor Controller [17]

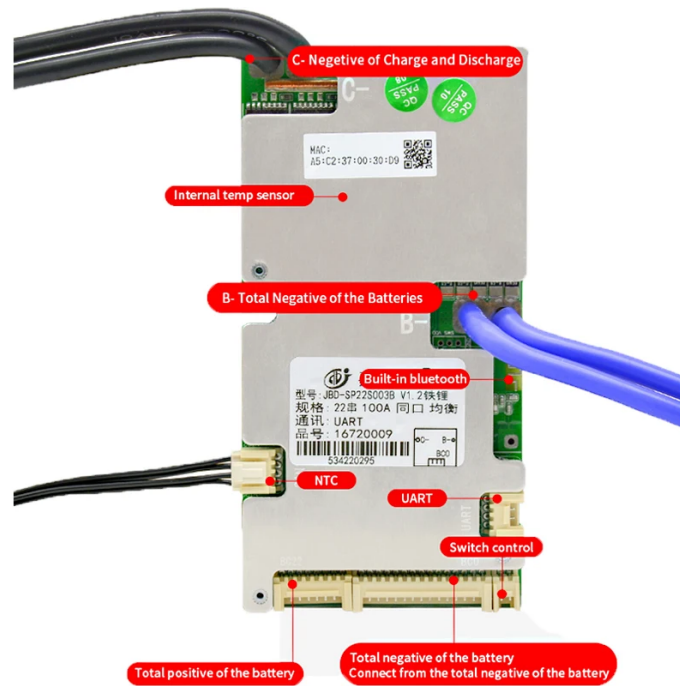


Fig. 21: selected BMS model JIABAIDA 10S-17S 80A

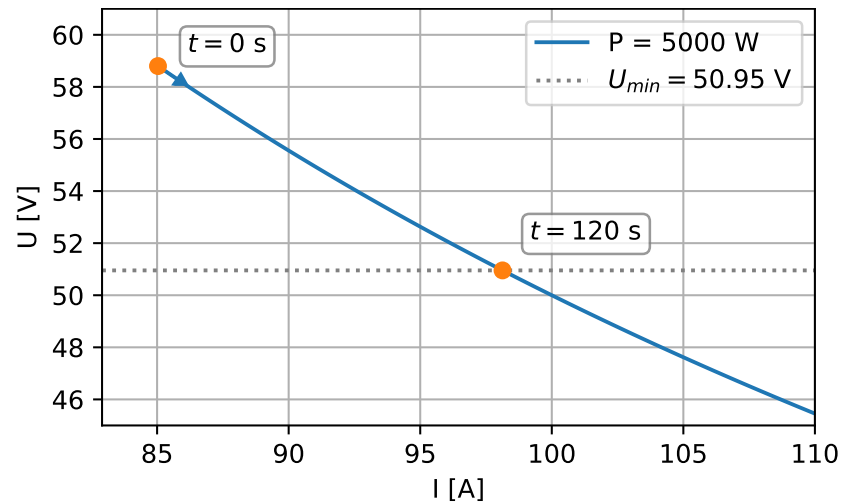


Fig. 22: Voltage and current of the battery pack over the flight time at constant power

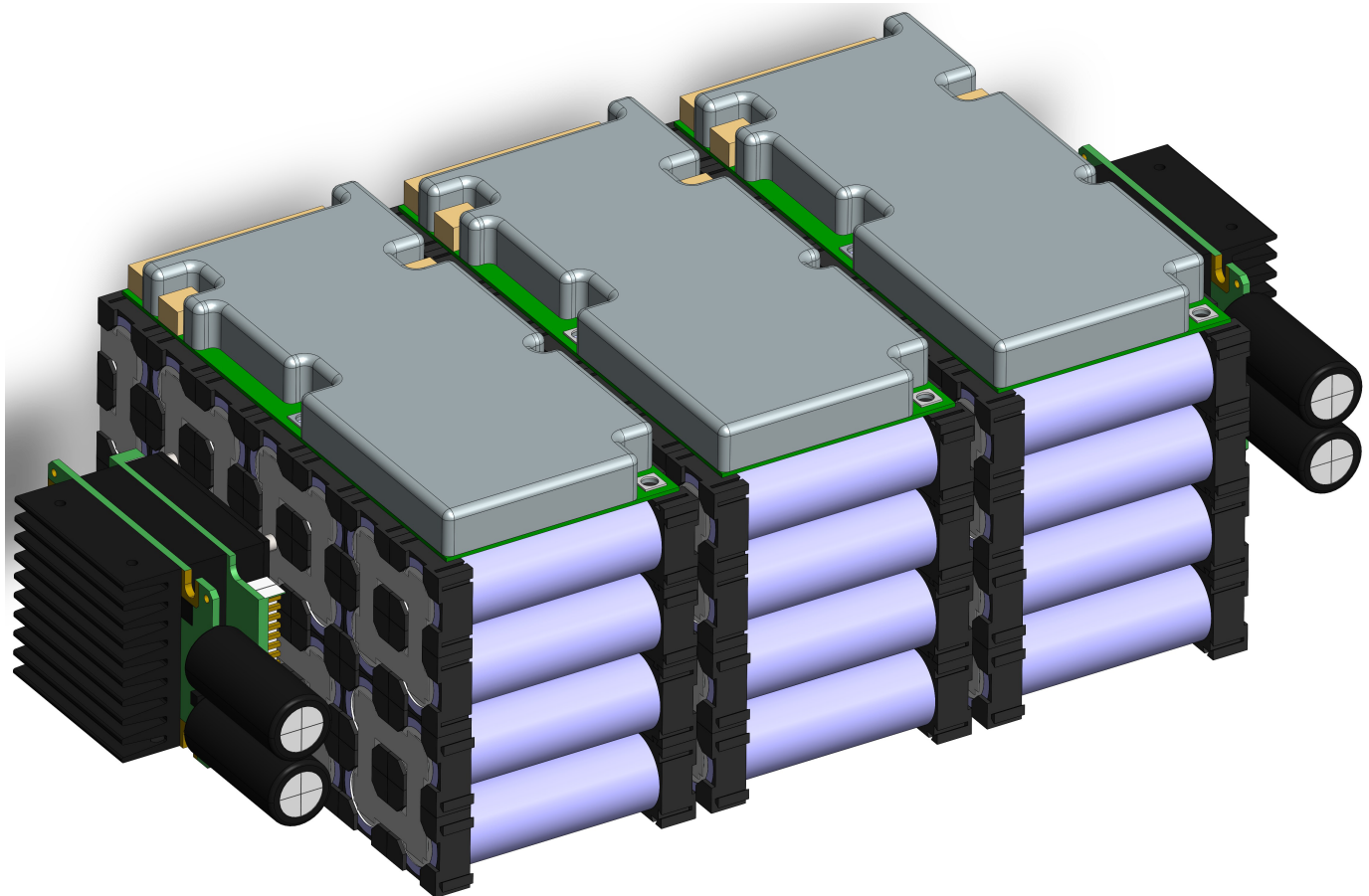
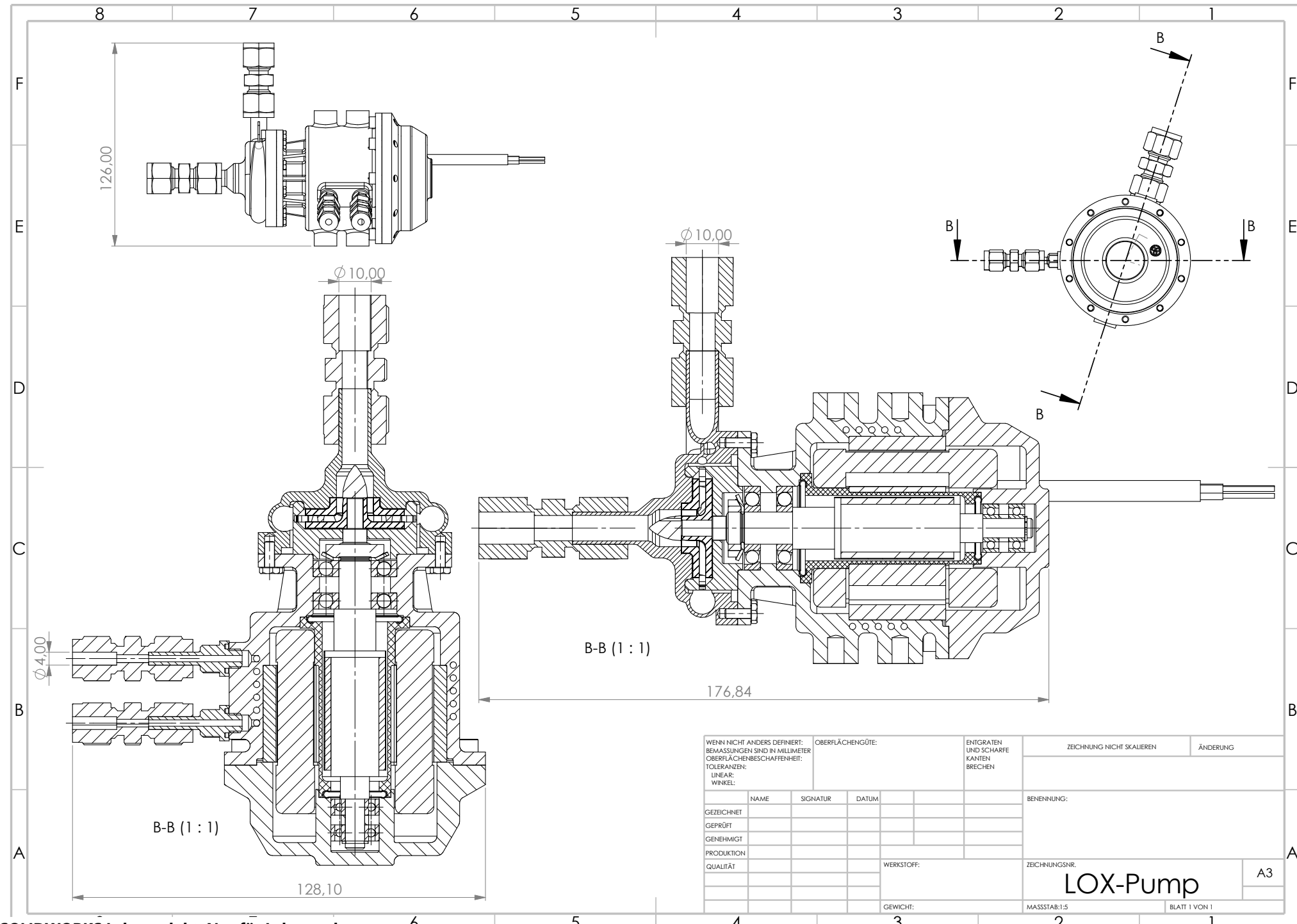
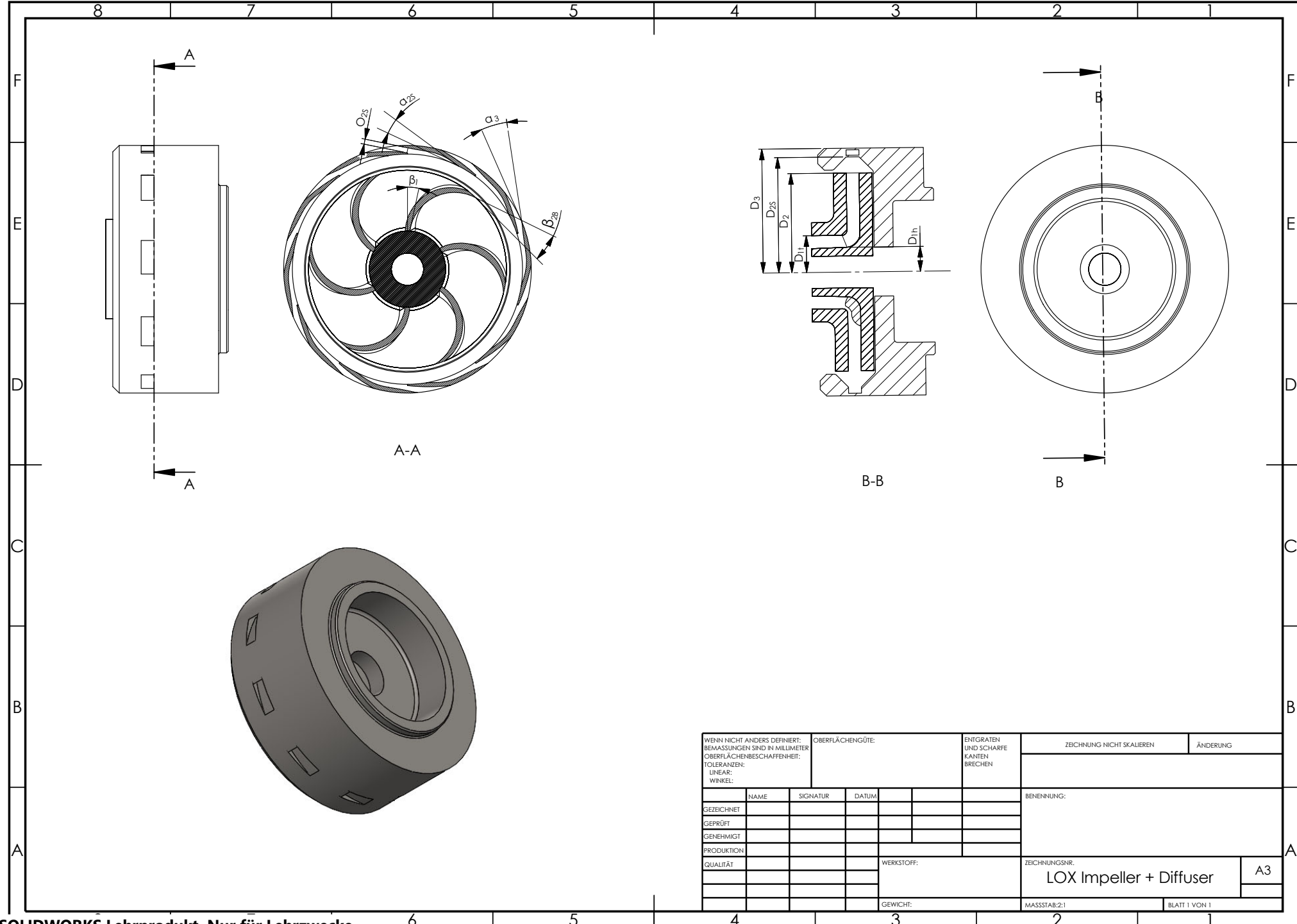


Fig. 23: Electric assembly of 14 S, 6 Pa, battery pack with 3 BMS and 2 BLDC drivers

F. LOX Pump Drawings





G. Eigenfrequency Analysis

Modellname: LOX-Pump
Studienname: Frequenz 1(-Default-)
Darstellungsart: Frequenz Amplitude1
Schwingungsform: 1 Wert= 314 Hz
Verformungsfaktor: 0,00208966

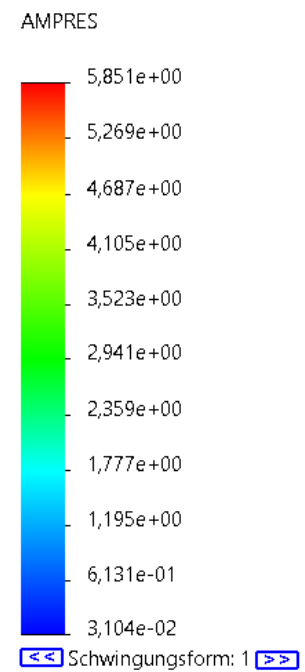


Fig. 24: Mode of first eigenfrequency at 314 Hz